Journal of Rock Mechanics and Geotechnical Engineering 16 (2024) 4335–4353

Contents lists available at ScienceDirect

Journal of Rock Mechanics and Geotechnical Engineering

journal homepage: www.jrmge.cn

Full Length Article

A coupled cryogenic thermo-hydro-mechanical model for frozen medium: Theory and implementation in FDEM

Lei Sun [a, b], Xuhai Tang [b], Kareem Ramzy Aboayanah [a], Qi Zhao [c, *], Quansheng Liu [b], Giovanni Grasselli [a]

[a] Department of Civil and Mineral Engineering, University of Toronto, Toronto, ON, M5S 1A4, Canada
[b] School of Civil Engineering, Wuhan University, Wuhan, 430072, China
[c] Department of Civil and Environmental Engineering, The Hong Kong Polytechnic University, Hung Hom, Hong Kong, China

ARTICLE INFO

Article history:
Received 19 February 2023
Received in revised form
3 August 2023
Accepted 4 September 2023
Available online 13 November 2023

Keywords:
Thermo-hydro-mechanical (THM) coupling
Low temperature
Heat transfer
Water migration
Frost heave
Combined finite-discrete element method (FDEM)

ABSTRACT

This paper presents the development of a coupled modeling approach to simulate cryogenic thermo-hydro-mechanical (THM) processes associated with a freezing medium, which is then implemented in the combined finite-discrete element method code (FDEM) for multi-physics simulation. The governing equations are deduced based on energy and mass conservation, and static equilibrium equations, considering water/ice phase change, where the strong couplings between multi-fields are supplemented by critical coupling parameters (e.g. unfrozen water content, permeability, and thermal conductivity). The proposed model is validated against laboratory and field experiments. Results show that the cryogenic THM model can well predict the evolution of strongly coupled processes observed in frozen media (e.g. heat transfer, water migration, and frost heave deformation), while also capturing, as emergent properties of the model, important phenomena (e.g. latent heat, cryogenic suction, ice expansion and distinct three-zone distribution) caused by water/ice phase change at laboratory and field scales, which are difficult to be all revealed by existing THM models. The novel modeling framework presents a gateway to further understanding and predicting the multi-physical coupling behavior of frozen media in cold regions.

1. Introduction

A quarter of the continental surface is occupied by permafrost, and over half of the continental surface experiences seasonal freezing (Streletskiy et al., 2018; Obu et al., 2019; Sun et al., 2022a). Frost weathering, a fundamental geomorphic process in cold regions (from polar regions to tropical high mountains), significantly influences the geomorphology (periglacial landforms evolution (Gruber and Haeberli, 2007; Matsuoka and Murton, 2008)), geo-disasters (rockfall, debris flow (Harris et al., 2009; Fischer, 2009)), and geotechnical engineering (tunnel, pipeline, underground liquefied gas storage, artificial ground freezing, and CO_2 sequestration (Tan et al., 2013; Lai et al., 2014; Xia et al., 2018; Deprez et al., 2020; Huang et al., 2020)), which are exacerbated by climate changes (Gruber and Haeberli, 2007; Harris et al., 2009; Sun et al., 2023a). Generally, frost weathering is a typical thermo-hydro-mechanical (THM) coupled problem, which involves constant and complex interactions between the thermal, hydraulic, and mechanical processes (Nishimura et al., 2009; Kang et al., 2013; Bekele et al., 2017; Huang et al., 2018a). For example, phase changes of pore fluid caused by temperature variations modify the hydraulic regime of the material, which in turn induces mechanical deformation. Meanwhile, changes in the hydraulic and mechanical conditions feed back into the thermal processes by means of advection and changes in water/ice contents (Nishimura et al., 2009; Duca et al., 2015). Therefore, a proper THM coupling model considering the strong coupling effect between multi-fields is of great significance to the freezing problems in engineering applications.

Numerical techniques (Jing and Hudson, 2002; Arzanfudi and Al-Khoury, 2018; Wu et al., 2020a) are usually adopted to solve coupled problems, because of the strong mutual interaction

* Corresponding author.
E-mail address: qi.qz.zhao@polyu.edu.hk (Q. Zhao).
Peer review under responsibility of Institute of Rock and Soil Mechanics, Chinese Academy of Sciences.

https://doi.org/10.1016/j.jrmge.2023.09.007

between the multi-fields, and the related highly non-linear mathematical equations, as well as complex boundary conditions. To date, numerous THM coupling models have been developed to simulate coupled processes associated with various engineering applications, such as geothermal energy extraction, nuclear waste storage, and oil/gas exploitation (Rutqvist et al., 2001; Hudson et al., 2005; Tong et al., 2010; Nowak et al., 2011; Yan et al., 2022). However, most of the published THM models focus on normal/high temperature and are not directly applicable to low temperature conditions. One primary distinction of the cryogenic THM coupled process is its ability to account for the water/ice phase change (PC), which introduces complicated coupling mechanisms (Kang et al., 2013; Huang et al., 2018a). Firstly, the water/ice phase change induces latent heat, which influences the temperature field. Secondly, a negative pore pressure (known as cryogenic suction) induced by the change in ice/water content gives rise to water migration. In addition, ice generation changes the content of the mixture system, affecting the material properties (e.g. thermal/physical/mechanical properties). For example, pore ice promotes heat conduction but prevents water seepage, as a result the equivalent thermal conductivity increases while the permeability decreases with the increase in ice content. Finally, the water/ice transition is also associated with a volumetric change (expansion during freezing, and volume reduction during thawing).

In recent decades, THM coupling models at low temperatures have drawn increasing interest and have been developed and tailored to particular applications. Harlan (1973) first proposed a thermo-hydraulic (TH) model to predict water flow and temperature field in partially frozen soil considering the interaction of heat and fluid transport. Taylor and Luthin (1978) and Guymon et al. (1980) improved the TH model to account for the frost heave process. Subsequently, Fremond and Mikkola (1991) established a thermo-mechanical (TM) model to describe the frost heave of freezing soil based on the principles of continuum mechanics and macroscopic thermomechanics. Michalowski and Zhu (2006), Yang et al. (2006), and Cai et al. (2019) further developed the TM coupling model and applied it to practical engineering problems. Wu et al. (2019, 2020b, 2022a, b) developed a hydro-mechanical (HM) model for elasto-plastic porous media, considering both saturated and semi-saturated seepage. For coupled multi-field models, Mu and Ladanyi (1987) first proposed a simplified THM coupled model and implemented it in a finite difference numerical simulator. The pore pressure was evaluated using the Clausius-Clapeyron equation, and the frost heave deformation was described by additional volumetric expansion related to density change due to the phase transition and water accumulation behind the freezing front. Suh and Sun (2022), Na (2018), Sweidan et al. (2020) and Lu et al. (2011) developed a phase-field THM model that simulates the growth and thaw of ice lenses and the resultant frozen heave and thaw settlement in multi-constituent frozen soils. Recently, more low-temperature THM models (Neaupane and Yamabe, 2001; Nishimura et al., 2009; Liu and Yu, 2011; Lai et al., 2014; Duca et al., 2015; Na and Sun, 2017; Huang et al., 2018a; Zhelnin et al., 2022) have been developed and implemented with varying hypotheses and degrees of sophistication. However, the strong coupling between the multi-field at low temperature, especially considering the water/ice phase change is still far from being fully understood. The aforementioned models still individually encounter obstacles to realistically capture all the concerned phenomena (e.g. temperature field, water redistribution, frost heave) observed in the field and laboratory experiments.

Recently, a state-of-the-art numerical method, the combined finite-discrete element method (FDEM) (Munjiza, 2004), which incorporates the advantages of both continuum and discontinuum methods, has attracted extensive research interest and has been employed successfully in geotechnical engineering problems (Lisjak et al., 2018; Knight et al., 2020; Fukuda et al., 2020; Sun et al., 2022b). The FDEM has also been extended to multi-field coupled problems, e.g. HM, TM, and THM models (Lei et al., 2014; Lisjak et al., 2017; Yan and Jiao, 2019; Sun et al., 2020; Yan et al., 2022). This paper aims to extend the FDEM, with the aid of a cryogenic THM coupled model, to investigate the coupled multi-physics behaviors of a frozen medium at low temperatures. Specifically, the water/ice phase transition at low temperature is intuitively considered, and critical coupling parameters are established to control the strong coupling between multi-fields. Unlike the previous modeling efforts in which some important mechanisms (e.g. flow of unfrozen water, energy dissipation due to phase transition, or property variation) are neglected more or less (Harlan, 1973; Mu and Ladanyi, 1987; Fremond and Mikkola, 1991), all important physical and thermodynamic phenomena and processes occurring at low temperatures (e.g. heat transfer, water/ice phase change, latent heat of phase transition, cryogenic suction, frost heave, and water migration, as well as the critical coupling parameters) are addressed in the model.

The paper is organized as follows. In Section 2, a theoretical framework is established to formulate the cryogenic THM model, along with governing equations and key coupling parameters. In Section 3, the implementation of the THM coupled model into FDEM and the coupling procedure is illustrated in detail. In Section 4, validation tests are conducted to demonstrate the accuracy and computational capability of the proposed model against existing benchmark cases. Lastly, a field-scale experiment of a chilled pipeline is numerically investigated utilizing the proposed model, and the effects of water migration and insulation material are discussed. The discussion and conclusions of this work are outlined in Sections 5 and 6, respectively.

2. Basic theory of the cryogenic THM coupled model

2.1. Coupling mechanism

As shown in Fig. 1, thermal, hydraulic, and mechanical fields in the frozen medium strongly interact with each other. When the temperature stays above the freezing level, the thermal field would affect the hydraulic field by changing fluid properties and be affected by fluid heat transport in return. The hydraulic field would influence the mechanical field through pore pressure and be affected by bulk strain. The mechanical field would affect the thermal field through mechanical work and bulk strain and be affected by thermal stress. Especially, when the temperature drops to a subfreezing level, water/ice phase change occurs, leading to a more complicated transient coupling mechanism. Firstly, the latent heat would influence the thermal field, while the volume expansion caused by the ice growth would exert additional pressure (called freezing pressure or ice pressure) altering the mechanical field. Furthermore, the ice generation would induce a driving force (i.e. cryogenic suction) to local water migration, as well as significantly affect the hydraulic conductivity. Ultimately, the change in phase and pore structure will greatly affect the material characteristics (e.g. hydraulic, thermal, and mechanical properties), thus further impacting the multi-physical response. The strong coupling of THM behavior in response to the freezing process necessitates considering all aforementioned processes and implementing proper constitutive relationships in the numerical model.

2.2. Governing equations

The governing equations of the proposed cryogenic THM coupled model are derived from the mass and energy conservation

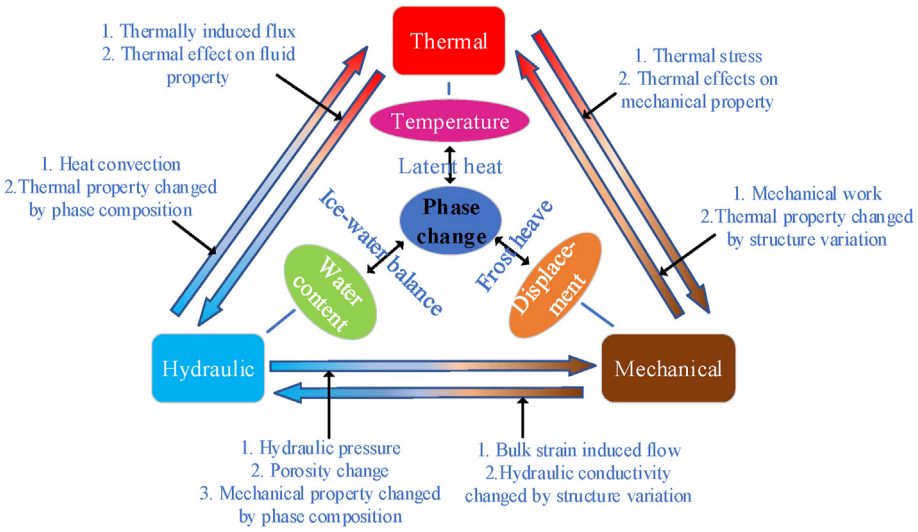

Fig. 1. Schematic representation of cryogenic THM coupling.

and static equilibrium equations. Considering the complex multi-field coupled process, the following assumptions are made to facilitate this model (Kang et al., 2013; Lai et al., 2014; Huang et al., 2018a): (1) The porous medium is considered an isotropic and elastic material that is fully saturated with water/ice; (2) The pore ice is immobile relative to the solid skeleton; (3) Local thermal equilibrium between the three phases is assumed (i.e. all the phases have the same temperature); (4) As the deformation rate is rather low for quasi-static problems, the influence of material deformation on temperature change is insignificant; (5) The freezing point of pore water is assumed as $T_0 = 0$ °C and remains constant (i.e. the freezing point depression due to loading and pore water salinity is negligible); (6) The material properties of the frozen medium vary with the material contents, described by the theory of mixture.

2.2.1. Energy conservation

The energy conservation equation of a variably saturated medium is described as (Nassar and Horton, 1992; Rouabhi et al., 2018):

$$C_e\frac{\partial T}{\partial t}+\nabla\cdot\boldsymbol{q}_t+q_{ph}+C_l\boldsymbol{q}_l\nabla T=q_{st} \tag{1}$$

where T is the temperature; t is the time; C_e and C_l are the volumetric thermal capacity of the mixture system and the liquid water phase, respectively; $\boldsymbol{q}_l$ is the water flux vector; $\boldsymbol{q}_t$ is the heat flux; q_{st} is the source term (sink/production term of energy); and q_{ph} is the latent heat due to water/ice phase change. The heat flux $\boldsymbol{q}_t$ can be expressed using Fourier's law as

$$\boldsymbol{q}_t=-k_e\nabla T \tag{2}$$

where k_e is the equivalent thermal conductivity.

In addition, the latent heat generated by water/ice phase change is (Huang et al., 2018a):

$$q_{ph}=\rho_l L\frac{\partial\theta_l}{\partial t} \tag{3}$$

where ρ_l is the density of water, L is the latent heat coefficient, and θ_l is the unfrozen water content.

To reduce the non-linearity and avoid numerical difficulties, the concept of apparent heat capacity C_a is introduced to incorporate the phase change, and Eq. (1) can be rewritten as (Zhang et al., 2021):

$$C_a\frac{\partial T}{\partial t}-\nabla\cdot(k_e\nabla T)+C_l\boldsymbol{q}_l\nabla T=q_{st} \tag{4}$$

where

$$C_a=\begin{cases}C_e+L\rho_l\dfrac{\partial\theta_l}{\partial T} & (T\le T_0)\\ C_e & (T>T_0)\end{cases} \tag{5}$$

where $T_0 = 0$ °C is the freezing point of pore water. Coupling variables C_e and k_e are temperature-dependent and will be introduced in Section 2.3 in detail.

2.2.2. Mass conservation

The solid phases are assumed to be stationary during the freezing process, and only the water phase can flow. Thus, mass conservation of variably saturated water flow for both above- and sub-zero temperature is (Hansson et al., 2004; Huang et al., 2018a):

$$n\frac{\partial}{\partial t}(\rho_l S_l+\rho_i S_i)-\nabla(\rho_l\boldsymbol{q}_l)=q_{sh} \tag{6}$$

where n is the porosity; S_l and S_i are the saturation degrees of water and ice phases, respectively, and $S_l + S_i = 1$; $\boldsymbol{q}_l$ is the water flux vector; and q_{sh} is the sink/source term of fluid mass. According to the modified Richards equation (Hansson et al., 2004; Liu and Yu, 2011), the water flux, $\boldsymbol{q}_l$, can be calculated as

$$\boldsymbol{q}_l=K_{LH}\nabla H+K_{LT}\nabla T \tag{7}$$

where $H = h + z$ is the total pressure head, in which h is the pore pressure head and z is the gravity potential head; K_{LH} and K_{LT} are the hydraulic conductivity for liquid phase fluxes due to pressure gradient and temperature gradient, respectively, which are related to the liquid saturation degree and will be introduced in Section 2.3 in detail.

Based on the generalized Clapeyron equation (Williams and Smith, 2009), which is used to describe the thermodynamic equilibrium of the coexistence between water and ice, the pressure

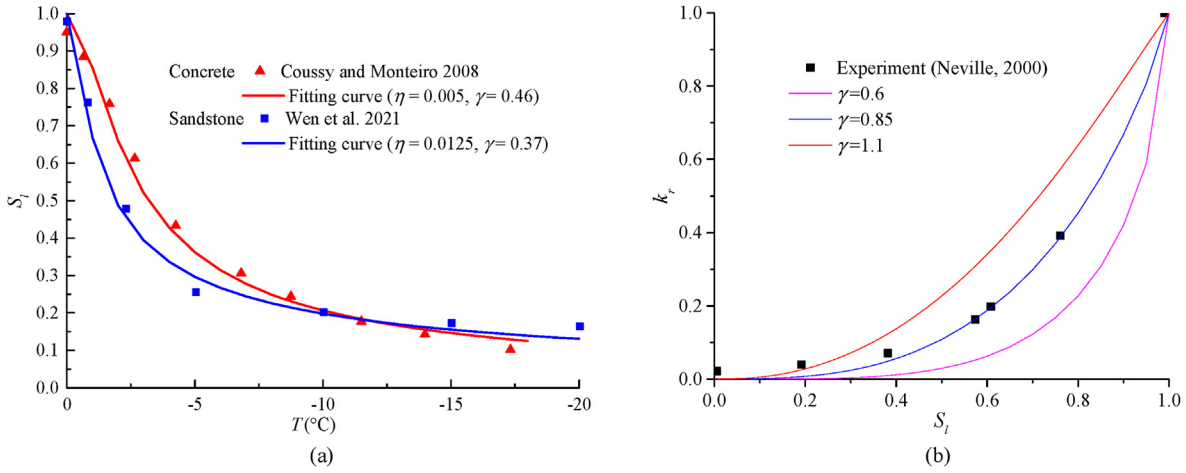

Fig. 2. Fitting curves of (a) unfrozen water degree versus temperature (Coussy and Monteiro, 2008; Weng et al., 2021) and (b) relative hydraulic conductivity versus unfrozen water degree (Neville, 1995).

head (i.e. cryogenic suction) at subzero temperature can be related to the temperature as (Hansson et al., 2004; Kurylyk and Watanabe, 2013; Deprez et al., 2020):

$$h = L\ln\left(\frac{T+273.15}{T_0+273.15}\right)\Big/ g \tag{8}$$

where L is the specific latent heat, g is the gravity acceleration, and T is the temperature in degrees Celsius. From the above, a negative pore pressure of 11–12 atm is generated by every degree Celsius below zero (Deprez et al., 2020).

2.2.3. Mechanical equilibrium

The frozen formation is assumed to be a continuous isotropic medium. The equilibrium equation can be expressed as (Coussy, 2005; Huang et al., 2018a):

$$\nabla\boldsymbol{\sigma} + \boldsymbol{b} = 0 \tag{9}$$

where $\boldsymbol{\sigma}$ are the total stresses and $\boldsymbol{b}$ are the body forces.

The stress is further linked to strain via a constitutive model (Liu and Yu, 2011; Bekele et al., 2017):

$$\boldsymbol{\sigma} = \boldsymbol{D}\left(\boldsymbol{\varepsilon} - \boldsymbol{\varepsilon}^{\mathrm{PC}} - \boldsymbol{\varepsilon}^{\mathrm{T}} - \boldsymbol{\varepsilon}^{\mathrm{h}} - \boldsymbol{\varepsilon}^{\mathrm{q}}\right) \tag{10}$$

where $\boldsymbol{D}$ is the stiffness matrix, $\boldsymbol{\varepsilon}$ is the total strain, $\boldsymbol{\varepsilon}^{\mathrm{PC}}$ is the strain due to phase change, $\boldsymbol{\varepsilon}^{\mathrm{T}}$ is the thermal strain due to temperature change, $\boldsymbol{\varepsilon}^{\mathrm{h}}$ is the strain due to matric potential, and $\boldsymbol{\varepsilon}^{\mathrm{q}}$ is the strain due to water accumulation.

2.3. Critical coupling parameters

The governing equations of the coupled THM model for frozen media are introduced above, where the coupling effect between multiple fields during the freezing process is mainly reflected by the critical coupling parameters. Thus, supplementary equations are provided, including unfrozen water degree and equivalent material properties (e.g. equivalent permeability and thermal conductivity).

2.3.1. Unfrozen water degree

Although water transitions to ice at subfreezing temperatures, considerable unfrozen water still exists in rock masses (Johannesson, 2010; Zhou et al., 2014). This phenomenon is a key coupling parameter that has a significant impact on the material's thermal-hydro-mechanical properties and thus affects the corresponding frozen behavior (Huang et al., 2018a; Zhelnin et al., 2022).

The relationship between subzero temperature and unfrozen water degree, for a given frozen medium, can be derived from the soil freezing characteristic curve (SFCC). To date, many SFCC models have been developed (Liu and Yu, 2011; Bai et al., 2020; Stuurop et al., 2021). In this study, the widely applied van Genuchten model (van Genuchten, 1980; Bekele et al., 2017) was used to represent the freezing characteristic function for the unfrozen water degree (S_l) (i.e. volume of liquid phase/volume of pore):

$$S_l = \left[1 + |\eta h|^{\frac{1}{1-\gamma}}\right]^{-\gamma} \tag{11}$$

where η and γ are the material constants, and η is the matric

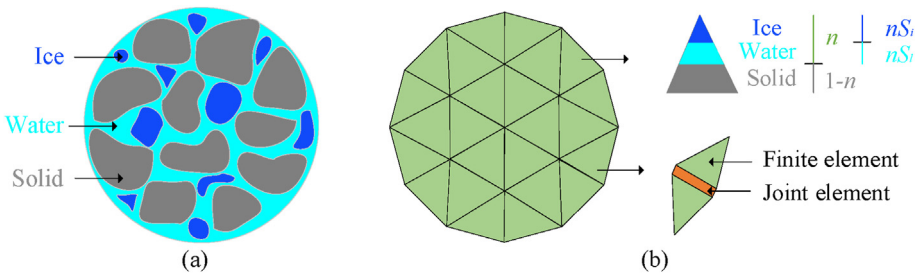

Fig. 3. (a) Schematic diagram of freezing medium containing three phases and (b) numerical representation of FDEM model. The volume fraction (content) of solid, water, and ice are $\theta_s = 1-n$, $\theta_l = nS_l$, and $\theta_i = nS_i$, respectively.

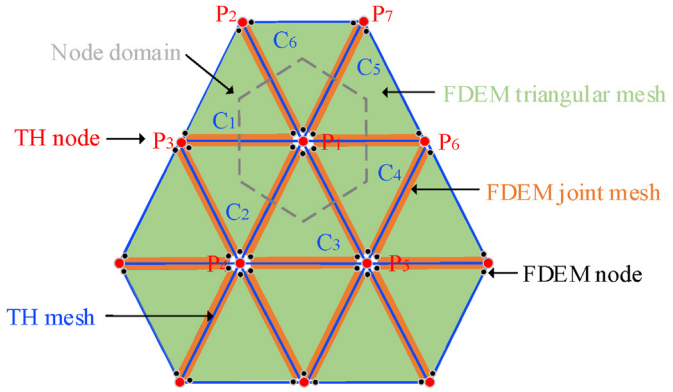

Fig. 4. Schematic diagram of the computational meshes: FDEM mesh (in green and orange) and TH mesh (in blue) for mechanical and thermo-hydraulic calculation respectively (P represents TH node and C represent TH mesh).

suction potential.

By substituting the Clapeyron relation (Eq. (8)) into Eq. (11), the freezing characteristic function relating S_l to T can be obtained as

$$S_l = \left[1 + |\eta L \ln(1 + T/273.15)/g|^{\frac{1}{1-\gamma}}\right]^{-\gamma} \tag{12}$$

It is shown that the unfrozen water degree is related to the temperature: the lower the temperature, the less water remains unfrozen. The model parameters η and γ can be selected for a given material based on experimental data, as shown in Fig. 2a.

2.3.2. Effective hydraulic conductivity

It is evident that at low temperatures, ice forms in the pores causing a blockage in the original water flow channel, resulting in lower permeability. The experimental results from Burt and Williams (1976) show that the hydraulic conductivity drops by 10^{-4} times below the original value within a narrow temperature range below the freezing point. Effective hydraulic conductivity, K_{LH}, can be derived from the van Genuchten model, as a function of the unfrozen water degree (Hansson et al., 2004; Bai et al., 2020):

$$K_{LH} = k_r K_s = K_s \sqrt{S_l}\left[1 - \left(1 - S_l^{1/\gamma}\right)^{\gamma}\right]^2 \tag{13}$$

where k_r is the relative hydraulic conductivity, K_s is the saturated hydraulic conductivity, S_l is the unfrozen water degree, and parameter γ is a material constant that in principle coincides with the parameter used in Eq. (11).

The hydraulic conductivity for liquid phase fluxes, K_{LT}, due to a gradient in T is (Hansson et al., 2004; Saito et al., 2006):

$$K_{LT} = K_{LH}\left(hG_{wT}\frac{1}{\phi_0}\frac{d\phi}{dT}\right) \tag{14}$$

where G_{wT} is the gain factor; and f is the surface tension of soil water, evaluated as $\phi = 75.6 - 0.1425T - 2.38 \times 10^{-4}T^2$, and $\phi_0 = 71.89\ g/s^2$ is the surface tension at 25 °C.

Since the saturation is a function of temperature, the effective hydraulic conductivity can also be directly related to the temperature. The model parameters can be selected for a given soil based on experimental data of hydraulic conductivity, as shown in Fig. 2b, where the permeability dramatically changes with decreasing saturation.

2.3.3. Equivalent thermal conductivity

The mixture system experiencing subzero temperatures comprises three phases, namely solid grain, unfrozen water, and ice. Each of these phases has different thermal properties (heat capacity and thermal conductivity). Therefore, the thermal properties of the frozen mixture vary with the water-ice phase transition.

The equivalent thermal properties of the mixture system can be calculated by mixture theory (Bekele et al., 2017; Arzanfudi and Al-Khoury, 2018). In the present study, two widely used weighted equations for volumetric heat capacity (C_e) and thermal conductivity (k_e) are adopted (Lai et al., 2014; Zhang et al., 2018; Lv et al., 2020):

$$C_e = (1-n)c_s\rho_s + nS_l c_l \rho_l + n(1-S_l)c_i\rho_i \tag{15}$$

$$k_e = k_s^{(1-n)} + k_l^{nS_l} + k_i^{n(1-S_l)} \tag{16}$$

where c_j, ρ_j and k_j (j = l, i, s) are the heat capacity, density, and thermal conductivity for water (l), ice (i), and solid grains (s), respectively; n is the porosity; S_l is the unfrozen water degree; and $S_i = 1 - S_l$ is the frozen degree which represents the percentage of water that has transformed into ice.

2.3.4. Mechanical properties variation

The generation of ice crystals changes the structural composition of the material, thus influencing the mechanical properties of the mixture. The effective mechanical properties of the mixture are derived as a function of material composition (Tounsi et al., 2019; Zhelnin et al., 2022):

$$\lambda_e = nS_l\lambda_l + n(1-S_l)\lambda_i + (1-n)\lambda_s \tag{17}$$

where λ is the mechanical/thermal properties (e.g. density, Young's modulus, Poisson's ratio, thermal expansion coefficient); the subscript e, l, i, and s denote the properties of equivalent material, water, ice, and solid grain, respectively; n is the porosity; and S_l is the unfrozen water degree. It is noted that this equation is also suitable for conditions without ice generation when the temperature is above the freezing point (i.e. $S_l = 1$).

3. Implementation of the cryogenic THM model into FDEM

In this section, we mainly focus on the implementation of the cryogenic THM model into the FDEM numerical framework. Some basic principles of FDEM are briefly introduced, however, for more in-depth information, the reader is referred to published literature (Munjiza, 2004).

A conceptual model of a saturated porous medium subjected to freezing conditions is shown in Fig. 3. When the temperature is above the freezing point, only the water phase exists in pores. However, when the temperature drops below the freezing point, the porous medium initially containing a mixture of solid grain (s), and liquid water (l), experiences the growth of ice (i), which is a new solid phase that gradually replaces the liquid water. Based on the mixture theory (Bekele et al., 2017; Arzanfudi and Al-Khoury, 2018), at any given time, the sum of each distinct phase is assumed to occupy the whole volume and is distributed continuously over it, regardless of its heterogeneity. In the two-dimensional (2D) FDEM framework, the porous medium is approximated as a homogeneous and isotropic continuum, which is numerically discretized into 3-node triangular finite elements bonded by zero thickness 4-node joint elements (Fig. 3b). Pores are evenly distributed in the matrix with an implicit porosity n assigned to each element. The phases are distinct from each other by their physical properties, as well as their mass and volume

fractions. The water/ice phase transition process is implicitly represented in the matrix by changing the water/ice fraction (i.e. equivalent material properties).

The cryogenic THM model can be separated into three main modules: thermal, hydraulic, and mechanical modules. The thermal module is used to calculate the temperature field of the rock mass and captures the phase change when the water temperature drops to the freezing point T_0 (0 °C in the present study). The hydraulic module is utilized to simulate the water migration under varying thermal/hydraulic boundary conditions. The mechanical module is then used to simulate the mechanical response of the rock masses considering thermal stress, water pressure, and ice expansion. It is noted that any variation in temperature, water content, and water/ice ratio in pores inevitably changes the material properties, which in turn affects the abovementioned fields.

Based on the unique FDEM topological connection (i.e. finite triangular elements bonded by joint elements), a thermo-hydraulic (TH) mesh (a set of non-overlapping triangular TH elements with TH nodes) is introduced into the FDEM mesh to facilitate thermal/hydraulic field calculation (Fig. 4). The thermal transfer and water migration are calculated based on the TH mesh, while the mechanical behavior is calculated based on the original FDEM mesh. FDEM nodes that share the same TH node have the same pressure and temperature. Compared to the previous multi-field coupled models developed in the FDEM (Lisjak et al., 2017; Yan et al., 2021), where heat/fluid transfer was computed through unrealistic (virtual) joint elements, the TH mesh proposed herein eliminates the pressure/temperature jump between nodes across joint in a continuum and eliminates the needs of an artificial joint conductivity coefficient determined by trial-and-error method, thus, resulting in a more realistic TH field distribution. In addition, by ignoring the virtual joint elements, the calculation efficiency is significantly improved. The detailed calculations of the thermal, hydraulic, and mechanical fields are elaborated in the following sections.

3.1. Thermal field and heat transport

Generally, any change in the thermal field always triggers changes to the whole system in terms of a multi-physical process. As discussed in Section 2.1, both heat conduction and heat advection, together with latent heat present during phase transition need to be considered during a cryogenic calculation. In this section, a novel cryogenic heat transfer algorithm is developed and incorporated into the FDEM platform.

3.1.1. Heat conduction

Heat conduction takes place when a temperature difference exists within the computational domain. In the current implementation, when the temperature at TH nodes is different, heat conduction occurs between these nodes inside a TH mesh. According to the Fourier heat conduction law, the heat flow rate along the i direction, q_i^T, can be expressed as (Yan et al., 2022):

$$q_i^T = -k_{ij}\frac{\partial T}{\partial j} \quad (i,j=x,y) \tag{18}$$

where T is the temperature, and k_{ij} is the equivalent thermal conductivity tensor (Eq. (16)).

Assuming that the temperature field in a TH mesh obeys a linear distribution, the temperature gradient in the triangular mesh is constant and can be expressed by Gauss' divergence theorem:

$$\frac{\partial T}{\partial i}=\frac{1}{A}\int_A \frac{\partial T}{\partial i}\mathrm{d}A=-\frac{1}{2A}\sum_{m=1}^{3} T_m n_i^m l^m \tag{19}$$

where A is the area of the triangular element; T_m is the temperature of the node m; l^m is the length of the triangular edge opposite to node m; $n_i^m=\boldsymbol{n}_m\bullet\boldsymbol{n}_i$ is the dot product of the $\boldsymbol{n}_m$ and $\boldsymbol{n}_i$, in which $\boldsymbol{n}_m$ is the outer normal of the triangular face opposite to node m, and $\boldsymbol{n}_i$ is the unit vector along i direction.

Thus, combining Eqs. (18) and (19), the heat flow rate, q_{cod}, into TH node m inside a TH mesh can be calculated by

$$q_{cod}=-\frac{q_i^T n_i^m l^m}{2} \quad (i=x,y) \tag{20}$$

3.1.2. Advective heat transfer

The advective heat transfer, q_{adv}, due to fluid flow can be calculated as (Bekele et al., 2017; Huang et al., 2018a):

$$q_{adv}=C_l\boldsymbol{v}\nabla T=C_l\left(q_x\frac{\partial T}{\partial x}+q_y\frac{\partial T}{\partial y}\right) \tag{21}$$

where q_x and q_y are the fluid flux in x and y directions, respectively, which will be introduced in detail in the hydraulic field (Section 3.2).

3.1.3. Latent heat

The latent heat, q_{ph}, generated by the water-ice phase change at each TH node is (Huang et al., 2018a):

$$q_{ph}=\xi\rho_l L\frac{\partial\theta_l}{\partial t} \tag{22}$$

where ρ_l is the density of water, L is the latent heat coefficient, θ_l is the unfrozen water content, t is the time, and ξ is the volumetric parameter expressed as (Bekele et al., 2017):

$$\xi=\frac{1}{3}\frac{n\rho_i\rho_l}{\rho_l S_l+\rho_i S_i} \tag{23}$$

where 1/3 means that the latent heat is evenly distributed over the three nodes in a TH mesh.

3.1.4. Temperature update

The total (net) heat flow, Q^T, of a TH node can then be calculated as the summation of heat flows, which comprises the conduction, advection, and latent heat in the surrounding TH meshes associated with the TH node:

$$Q^T=\sum_{np}(q_{cod}+q_{adv}+q_{ph})\Bigg) \tag{24}$$

where np is the total number of the surrounding elements.

The temperature at the TH node can be updated as

$$T_{t+\Delta t}=T_t+\frac{Q^T}{c_e M}\Delta t \tag{25}$$

where $T_{t+\Delta t}$ and T_t are the temperatures at the current and previous time steps, respectively; c_e is the equivalent specific heat capacity; and M is the mass of the node domain, which is 1/3 of the total mass of all connected TH meshes (Fig. 4). Note that the specific heat and density are temperature-dependent. Similarly, the temperature of

other discrete thermal nodes can be calculated, and the temperature field evolution can be obtained.

3.2. Hydraulic field and water migration

As discussed in Section 2.1.2, the water migration at low temperature is driven by fluid potential head gradient and thermal gradient. Similar to the thermal calculation, the fluid migration is also calculated using the TH meshes, where the hydraulic field is characterized by the pressure head at the discrete TH nodes.

3.2.1. Water flow due to pressure gradient

According to Darcy's law, for both frozen and unfrozen conditions, the fluid flux rate along the i ($i, j = x, y$) direction, q_i^H, due to pressure head, can be expressed as (Yan et al., 2022):

$$q_i^H = -K_{ij}\frac{\partial H}{\partial j} \tag{26}$$

where K_{ij} is the hydraulic conductivity of the mixture, which varies with the unfrozen water degree to reproduce the hindering effect of ice formation on the movement of the remaining liquid water in pores (Eq. (13)); H is the total pressure head of the solid matrix, including the pore pressure head (h) and gravity head (z), which is related to the water saturation and temperature at the nodes. When the temperature is higher than the freezing point, the pore is saturated with liquid water, and the pore pressure head has a positive value. However, when the temperature is below the freezing point, ice starts to grow and the pores become unsaturated with liquid water, where the pore pressure is equal to the cryogenic suction (Eq. (8)), i.e. a negative value. Thus, the pressure head (H) can be calculated as

$$H = \begin{cases} h + z & (T > T_0) \\ L\ln\left(\dfrac{T+273.15}{T_0+273.15}\right)\Big/ g + z & (T \le T_0) \end{cases} \tag{27}$$

Assuming the water pressure head field in a triangular element to be linearly distributed, the pressure head gradient in the triangular element is constant and can be expressed as

$$\frac{\partial H}{\partial i} = \frac{1}{A}\int_A \frac{\partial H}{\partial i} dA = -\frac{1}{2A}\sum_{i=1}^{3} H_m n_i^m l^m \tag{28}$$

where H is the pressure head of the node m, and parameters A, l^m and n_i^m are the same as those in Eq. (19).

Thus, the fluid flux driven by the fluid pressure, q_H, can be obtained:

$$q_H = -\frac{q_i^H n_i^{P_1} l^{P_1}}{2} \quad (i = x, y) \tag{29}$$

3.2.2. Water flow due to thermal gradient

In addition, the fluid flux due to the thermal gradient, q_T, can be calculated as

$$q_T = K_{LT}\boldsymbol{I}\nabla T \tag{30}$$

where T is the temperature field calculated in Section 3.1, and $\boldsymbol{I}$ is the identity matrix.

3.2.3. Water content update

The total (net) fluid flow, Q^H, of the TH node can then be calculated as the summation of fluid flow, which comprises the fluid pressure and thermal driven fluid flux, in the surrounding TH meshes associated with the node:

$$Q^H = \sum_{np}(q_H + q_T) \tag{31}$$

where np is the total number of the surrounding elements.

The water content at each node can be updated as

$$\theta_{t+\Delta t} = \theta_t + \frac{Q\Delta t - \Delta V}{V} \tag{32}$$

where $q_{t+\Delta t}$ and q_t are the water contents at the current and previous time steps, respectively; Δt is the time increase; V is the volume of this node domain at the current time step, which is 1/3 of the total volume of all connected TH elements (Fig. 4); and ΔV is the volume change between the current and the previous steps.

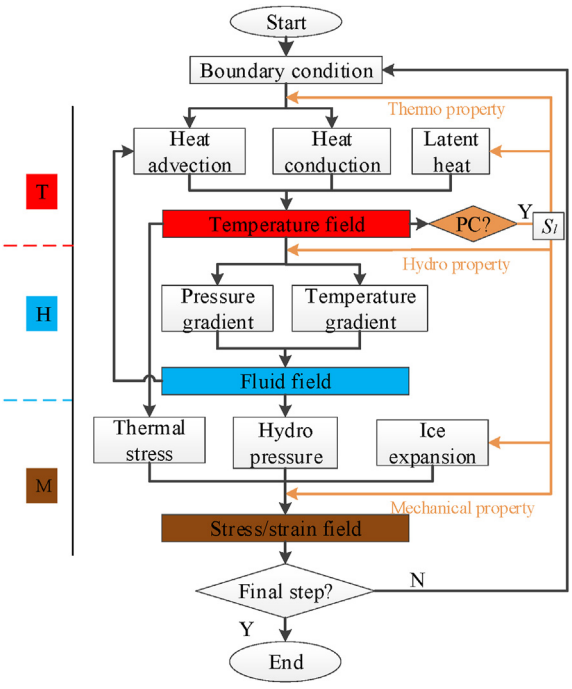

Fig. 5. Coupling procedure of the cryogenic THM model.

3.3. Mechanical field and frost deformation

We have assumed herein that all phases are incompressible and that the spatial variation of density (i.e. density gradient) is negligible for all phases. Generally, the deformation of the frozen medium can be attributed to four main parts: thermal stresses, water/ice phase change, cryogenic suction, and water accumulation (Liu and Yu, 2011; Huang et al., 2018a).

Any temperature change will induce thermal stress, and the corresponding thermal strain under both frozen and unfrozen conditions can be calculated as (Sun et al., 2020):

$$\Delta V^T = \left[(1+\alpha_e)^3 - 1\right]\Delta T \tag{33}$$

where ΔV^T is the thermal strain increment; and α_e is the thermal expansion coefficient, which can be calculated by Eq. (17) according to the specific phase composition of the mixture.

When the temperature drops below the freezing point, a water-ice phase change occurs, and the ice volume expansion induces significant volumetric strain. The volume expansion, ΔV^{PC}, due to ice formation considering the unfrozen water and water migration can be calculated as (Tan et al., 2018; Huang et al., 2018b):

$$\Delta V^{PC} = \beta(1 - S_l)(n + Q) \tag{34}$$

where n is the porosity, S_l is the unfrozen water degree that relates to the temperature, $\beta = 0.09$ is the volume expansion rate of water/ice phase change, and Q is the water migration flowing into the pores.

The strain resulting from the change of the matric potential, ΔV^h, is calculated by (Liu and Yu 2011):

$$\Delta V^h = h \Big/ H_m \tag{35}$$

where H_m is a material parameter similar to the modulus corresponding to matric potential, which can be obtained through experimental measurement (Fredlund and Rahardjo, 1993).

In addition, the inflow water migration also induces a pore structure variation, which affects the rock deformation. The volume change due to the extra water flow, ΔV^q, can be given as (Lai et al., 2014; Bai et al., 2020):

$$\Delta V^q = S - n \tag{36}$$

where $S = q_w + q_i = n(S_l + S_i)$ is the total water content, and n is the porosity. If $\Delta V^q < 0$, let $\Delta V^q = 0$.

An equivalent expansion coefficient, α_{eff}, is then introduced to calculate the corresponding equivalent stress of the mixture system (Huang et al., 2018a), considering all the aforementioned deformation during the freezing process:

$$\left(1 + \alpha_{eff}\Delta T\right)^3 = 1 + \Delta V \tag{37}$$

$$\Delta\sigma_{ij}^t = -3\delta_{ij}K\alpha_{eff}\Delta T \quad (i,j = x,y) \tag{38}$$

where ΔV is the total volume change, $\Delta\sigma_{ij}$ is the stress increment, δ_{ij} is Kronecker delta, and K is the equivalent bulk modulus.

The resulting equivalent stress is applied in the mechanical calculations as a volume force in the FDEM elements (Sun et al., 2023b), and allocated to the nodes of the triangular element. Then, the equivalent nodal force, $\boldsymbol{F}^n$, at an FDEM node can be given by

$$\boldsymbol{F}^n = \frac{1}{2}\boldsymbol{\sigma}\boldsymbol{n}l \tag{39}$$

where $\boldsymbol{\sigma}$ is the stress tensor; $\boldsymbol{n}$ and l are the normal unit vector and length of the triangular edge opposite to the node, respectively.

Finally, the geometry, deformation, and movement of the solid are given by the current coordinates of the nodes of the finite triangular element using Newton's second law (Munjiza 2004; Sun et al., 2022c):

$$\boldsymbol{M}\frac{\partial^2\boldsymbol{x}}{\partial t^2} + \boldsymbol{C}\frac{\partial\boldsymbol{x}}{\partial t} = \boldsymbol{F}(\boldsymbol{x}) \tag{40}$$

where $\boldsymbol{M}$ and $\boldsymbol{C}$ are the lumped mass and damping diagonal matrices of the system, respectively; $\boldsymbol{x}$ is the vector of the nodal coordinates; and $\boldsymbol{F}$ represents the total force vector of the node.

3.4. Boundary conditions

The initial condition can be given by

$$\boldsymbol{u}(x,y,0) = u_0 \tag{41}$$

where $\boldsymbol{u}$ is the variable in the governing equations, e.g. displacement, temperature, fluid pressure; and u_0 is a known function of time or a prescribed value of variable $\boldsymbol{u}$ at the initial time.

There are two types of boundary conditions included in the above model. The first type of condition is Dirichlet boundary condition:

$$\boldsymbol{u}|_\Gamma = u_s \tag{42}$$

where u_s is the prescribed value of variable $\boldsymbol{u}$ at the boundary G.

The second type of condition is Neumann boundary condition:

$$\frac{\partial u}{\partial \boldsymbol{n}}|_\Gamma = f_s \tag{43}$$

where $\boldsymbol{n}$ denotes the normal vector to the boundary, and f_s is a given scalar function at the boundary G.

3.5. Coupling procedure of the cryogenic THM model

A sequential coupling procedure between the multi-field is adopted to solve the cryogenic THM model, which can be decoupled into three sequential main parts: the thermal part, followed by the hydraulic part and the mechanical part (Fig. 5). At each calculation step, the thermal part is first performed to calculate the

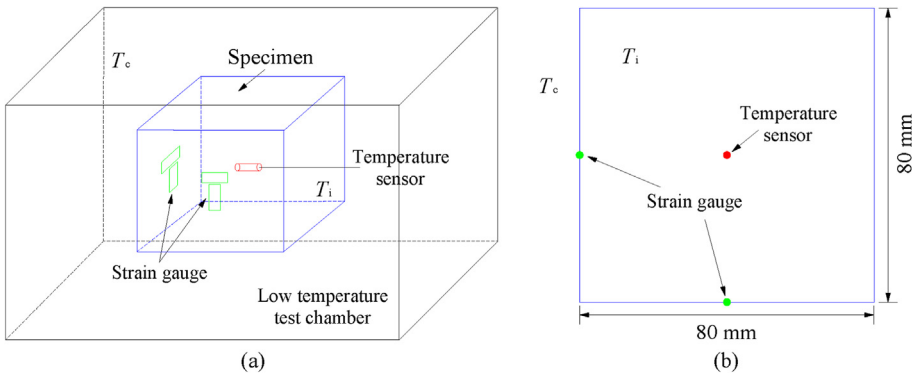

Fig. 6. (a) Schematic diagram of the specimen in low-temperature test chamber, and (b) the 2D numerical model.

Table 1
Test conditions.

Condition	Initial temperature, T_i (°C)	Chamber temperature, T_a (°C)	Moisture condition
I	20	−5	Dry
II	25	−5	Saturated
III	25	−10	Saturated

temperature field of the multi-phase porous medium. Then the frozen zone distribution, unfrozen water degree, and the corresponding thermal/hydraulic/mechanical property change as the temperature variation is obtained. The hydraulic module is then conducted to simulate the fluid field and water redistribution. Finally, the equivalent stress caused by the thermal/hydraulic field variation is applied to the mechanical part to calculate the stress/strain field. The updated geometry is then used to calculate the heat conduction at the next step. During the explicit iteration, the time step sizes used in the mechanical module and thermal/hydraulic module are different (Yan et al., 2022), and the thermal/hydraulic time, which has a physical meaning, is used in the following tests to show the sequence of simulation results.

It is noted that besides the direct coupling, the interaction between these three fields is also implicitly reflected by the material property change. During the iterative process, some interactions between different fields are realized at the current time step, while others are reflected at the next time step. For example, the thermal stress calculated from the temperature field and the fluid pressure calculated from the hydraulic field are used to update the mechanical field in the current time step. However, the fluid flux updated in the current time step is used to calculate the heat advection term in the thermal field in the next time step (Fig. 5). In this way, multiple interactions between three physics fields are updated iteratively.

4. Numerical tests

In this section, numerical examples are presented to validate the performance of the proposed cryogenic THM model in capturing the THM responses including the water/ice phase transition. The first test (Test 1) simulates a uniform freezing problem, and the simulated temperature and deformation fields are compared to experimental results. The coupling effect and the latent heat effect are highlighted in this test. In the second test (Test 2), the water migration and redistribution under the low temperature are verified against a well-known benchmark test. The model reproduces how the permeability changes with the varying temperature and recreates a three-zone distribution (i.e. frozen zone, freezing zone, and unfrozen zone). The third test model (Test 3) simulates the evolution of ground frost heave in the proximity of a chilled pipeline. We further discuss the water migration effect, as well as the impact of an insulating layer on the temperature distribution, water redistribution, and frost heave evolution.

4.1. Tests 1: uniform freezing of sandstone samples

The temperature field is a primary state variable in the overall THM coupling processes. In this section, a numerical simulation is carried out to validate the proposed model on the thermal transfer during the freezing process, as well as the corresponding frost strain, by comparing it with the laboratory experiment of Lv et al. (2018, 2019). Sandstone specimens, with the dimension of 80 mm × 80 mm × 80 mm (Fig. 6), were placed in a low-temperature test chamber under three different conditions as listed in Table 1. It is noted that the specimens in condition I was dried

Table 2
The basic thermomechanical parameters of sandstone and water/ice (after Lv et al., 2018).

Parameter	Value		
	Rock	Water	Ice
Density, ρ (kg/m^3)	2551	1000	917
Young's modulus, E (GPa)	2.3	–	9
Poisson's ratio, ν	0.24	–	0.3
Thermal conductivity, k (W/(m °C))	1.0	0.6	2.2
Specific heat capacity, c (J/(kg °C))	1735	4190	1920
Thermal expansion coefficient, α (°C^{-1})	18×10^{-6}	–	–
Porosity, n	0.184	–	–
Coupling parameters, η (m^{-1}) and γ	0.2, 0.5		
Convective heat transfer coefficient, k_c (W/(m^2 °C))	10		

before the experiment and served as a control test. The temperature variation and freezing strain were monitored by a temperature sensor and two pairs of strain gauges, respectively (Fig. 6a). Numerically, a 2D model is built in the FDEM simulator (Fig. 6b), where the two strain monitoring points are located at the middle of the boundary edge and a temperature monitoring point is located at the center of the specimen. The outer boundary is mechanically free, while a convective thermal boundary is applied (i.e. $q = k_c(T_a - T)$, where k_c is the convective heat transfer coefficient, T_a is the ambient temperature, and T is the temperature at boundaries). The simulation parameters are listed in Table 2.

The evolution of the temperature field and freezing strain under different conditions is shown in Fig. 7, where the numerical results are also compared with the experimental results of Lv et al. (2018). Overall, there is a good agreement between the simulation results and experimental results.

In the control test (i.e. condition I in Table 1, Fig. 7a), the temperature gradually decreases with time and stabilizes to a steady value (i.e. the chamber temperature). The slope of the temperature curve is sharp at first and becomes gentle as the temperature gradient decreases. Corresponding to the temperature decrease, the specimens experience thermal contraction and remain unchanged when the temperature reaches a stable value. It is noted that frost heave does not occur because of the zero water content (dry specimen).

For saturated specimens (i.e. conditions II (Fig. 7b) and III (Fig. 7c)), different variation trends of temperature and deformation can be observed. The temperature variation can be divided into four main stages: (i) the fast-cooling stage, where the temperature decreases rapidly; (ii) the phase change stage, where the temperature decreases much slower around the freezing point due to the release of the latent heat; (iii) the deep-cooling stage, where the temperature decreases faster than the phase change stage but slower than the fast-cooling stage; and (iv) steady stage, where the temperature tends to remain constant. It is also observed that the lower the chamber temperature, the quicker the temperature decreases, and the shorter the time during which the phase change stage is sustained. During the freezing process, thermal strain and ice expansion exist in the specimens simultaneously, inducing significant deformation. Three stages of strain variation are observed: the thermal contraction stage, the frost heaving stage, and the steady stage. The thermal contraction stage corresponds to the fast-cooling stage, where the temperature is positive and decreases to the freezing point, thus the strain is negative due to thermal contraction. The frost heaving stage corresponds to the later part of the phase change stage and the deep-cooling stage, where the pore water gradually changes to ice as the temperature falls below 0 °C; hence, the ice expansion induces the frost heave. The strain becomes positive as the ice expansion is dominant

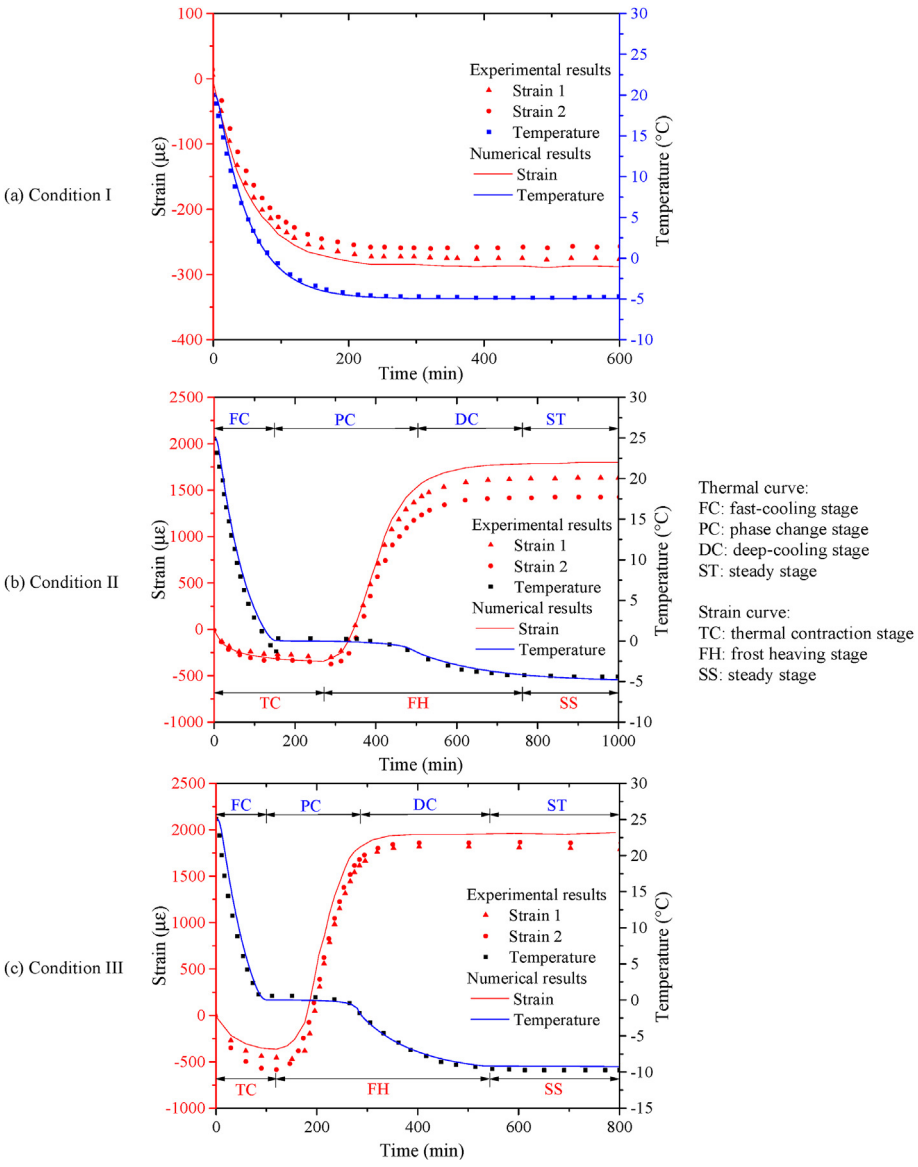

Fig. 7. The evolution of temperature and strain with time, and comparison with the experimental results (Lv et al., 2018). Since the numerical model is symmetric, only one simulation strain curve is presented.

during this stage. At the steady stage, the strain remains almost unchanged since the temperature tends to be stable. It is also found that in the lower chamber temperature condition (i.e. condition III), the strain decreases fast at thermal contraction stage and increases fast at the frost heaving stage. A larger frost heave deformation is observed in condition III, because more water transforms into ice under the lower temperature (i.e. less unfrozen water).

To better illustrate the heat transfer and frost heave process, the evolution of temperature and displacement distribution under condition III at different times are shown in Fig. 8. At $t = 50$ min, the temperature of the whole sample is higher than 0, thus only thermal contraction is observed. At $t = 200$ min, the temperature at the centre drops to 0 °C and the outer boundary is approximately −3 °C. An interesting finding is that contraction exists in the inner region, while expansion occurs in the outer part as the ice expansion (i.e. frost heave) becomes dominant as the displacement due to the fact that the frost heave is greater than the displacement due to thermal contraction. Then at $t = 300$ min and 600 min, the temperature drops further, and the frost heave further develops.

4.2. Test 2: water redistribution during the freezing process

Water migration and redistribution are key phenomena in the cryogenic THM coupling process. The benchmark test proposed by Mizoguchi (1990) is widely used as a verification test in many numerical models (Hansson et al., 2004; Tan et al., 2011; Liu and Yu, 2011; Wu et al., 2015), and it is adopted here to validate the simulated temperature field and frost-induced water redistribution.

In the experiment, Kanagawa sandy loam was packed in three identical cylinders, with a length of 20 cm and an internal diameter of 8 cm (Fig. 9). The specimens were prepared with the same initial conditions, which involved a uniform temperature of 6.7 °C and uniform volumetric water content of 0.33. The side and bottom faces of the cylinders were thermally insulated, and their top faces were exposed to a circulating fluid with a temperature of −6 °C (i.e. a convective boundary condition). All the outer boundaries are

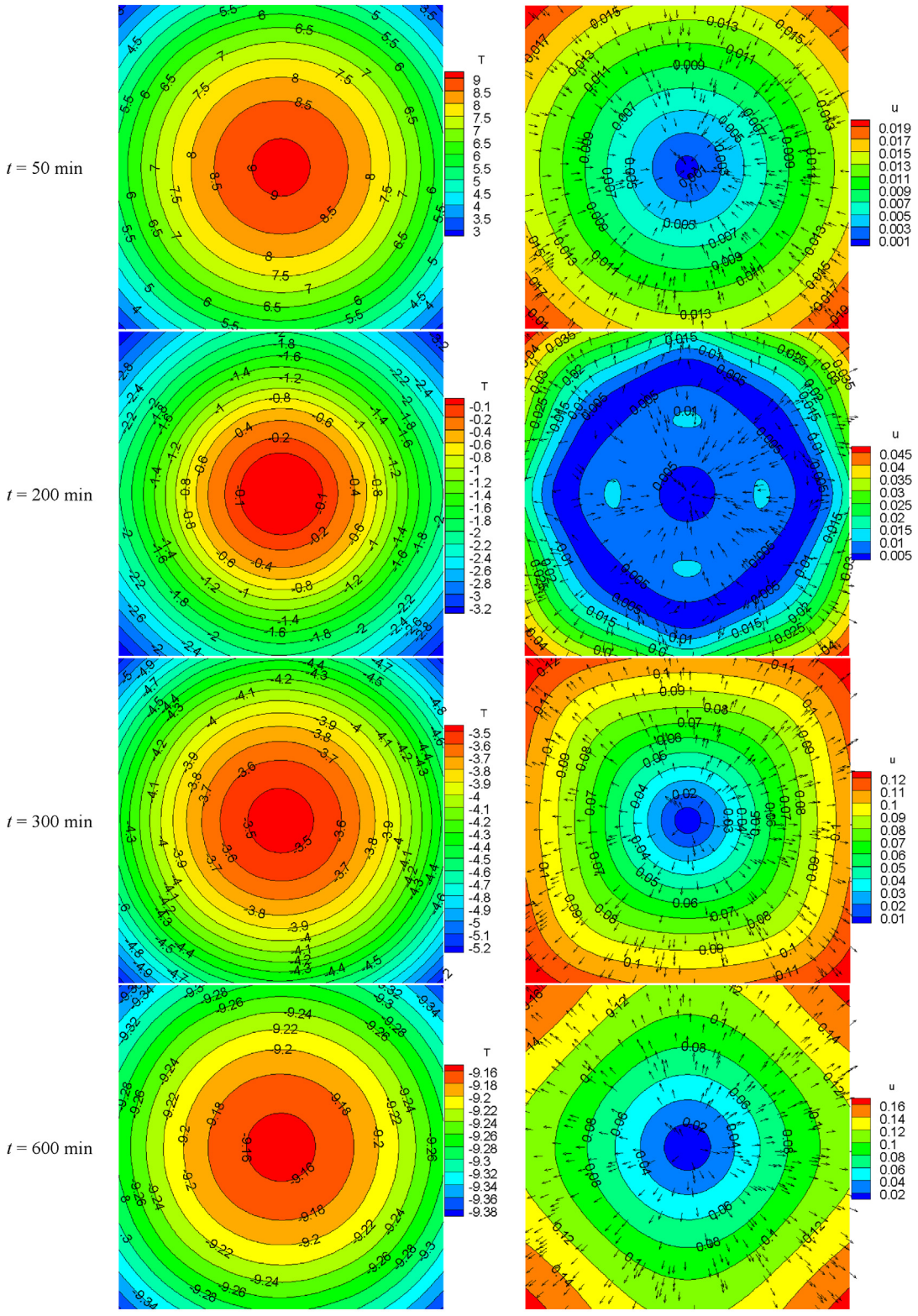

Fig. 8. Variations of (a) temperature (T, °C) and (b) displacement (u, mm) fields of Condition III at different times. Arrows indicate the deformation direction.

assumed to be impermeable. Then the specimens were removed from the cooling apparatus after 12 h, 24 h and 50 h, respectively, and the samples were then divided into 1 cm slices to obtain the total water content (liquid water content plus ice content) distributions. An axisymmetric numerical model is adopted to simulate the laboratory experiments, and the initial conditions are set to be the same as those in the experiments. The main parameters of the soil are listed in Table 3, and the parameters of water/ice

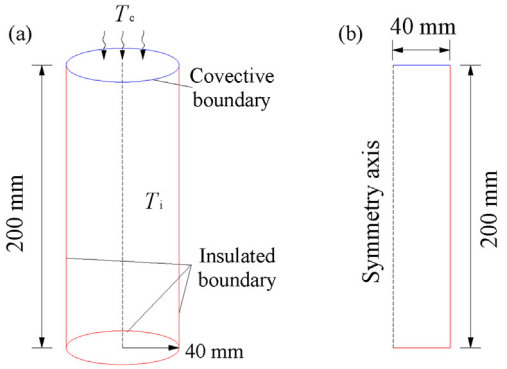

Fig. 9. Sketch of the (a) soil column and the (b) calculation model.

Table 3
The basic THM parameters of sandy loam (after Hansson et al., 2004; Tan et al., 2011; Wu et al., 2015).

Parameter	Value
Porosity, n	0.53
Density, ρ (kg/m^3)	2215
Thermal conductivity, k (W/(m °C))	1.62
Specific heat capacity, c (J/(kg °C))	850
Thermal expansion coefficient, α (°C^{-1})	8×10^{-7}
Convective coefficient, k_c (W/(m^2 °C))	28
Hydraulic conductivity, K_s (m/s)	3.2×10^{-6}
Coupling parameters, η (m^{-1}), γ	1.1, 0.25

are the same as those in Table 2.

The simulated temperature profiles at different times are shown in Fig. 10. The temperatures decrease gradually during the freezing process while the freezing front (i.e. 0 °C isothermal) propagates downwards since the specimens were frozen from the top. It can also be observed that the temperature decreases more rapidly (a larger temperature gradient) in the zone with subzero temperature than that in the zone with above-zero temperature, which is ascribed to the different heat conducting properties between the ice and water phases. Overall, the numerical results of the temperature distribution agree well with the experimental results.

As a result, the freezing process induces significant water redistribution within the samples. The distribution of the total water content (including both liquid water and solid ice) at different times (t = 0 h, 12 h, 24 h and 50 h) is shown in Fig. 11, where the moisture field curve can be divided into three parts: frozen, freezing, and unfrozen zones. In the frozen part, where the temperature is negative, the total moisture content is higher than the initial state and tends to remain unchanged. In the unfrozen part, where the temperature is higher than 0 °C, the total moisture content is lower than the initial value and decreases gradually towards the freezing front. The freezing zone (i.e. freezing fringe) exists between the frozen and unfrozen zone, where the temperature is near 0 °C and the total volumetric water content changes dramatically. The position of the minimum water content is primarily located near the freezing front (0 °C), which moves down gradually with increasing freezing time.

The comparisons between the numerical results by the proposed model and experimental results by Mizoguchi (1990) at different times are shown in Fig. 11. It is evident that the evolution of the calculated total water content in this study is fairly close to that of the experimental results. Specifically, the rapid decrease in the total water content at or immediately below the freezing front and the gradual recovery deeper in the columns are predicted well, as well as the shape transition at the freezing front. The rapid decrease of water content in the frozen fringe and the slow recovery at deeper positions are well predicted. In addition, the three-zone distribution (frozen, freezing, and unfrozen zones) observed in previous works (Konrad and Morgenstern, 1980; Zhou and Zhou, 2012; Lai et al., 2014; Deprez et al., 2020) can also be captured.

The redistribution of the water content can be explained by the variation of unfrozen water content and apparent hydraulic permeability, as shown in Fig. 12. During the freezing process, as the temperature decreases below the freezing point in the freezing zone, water transforms into the ice phase and the liquid water content decreases (although the total water content increases), thus inducing an extremely large matric potential head gradient (Eq. (8)), which is the driving force of the upward water migration from the unfrozen zone. Since the total water in a closed system is constant, the water migration results in the total water content

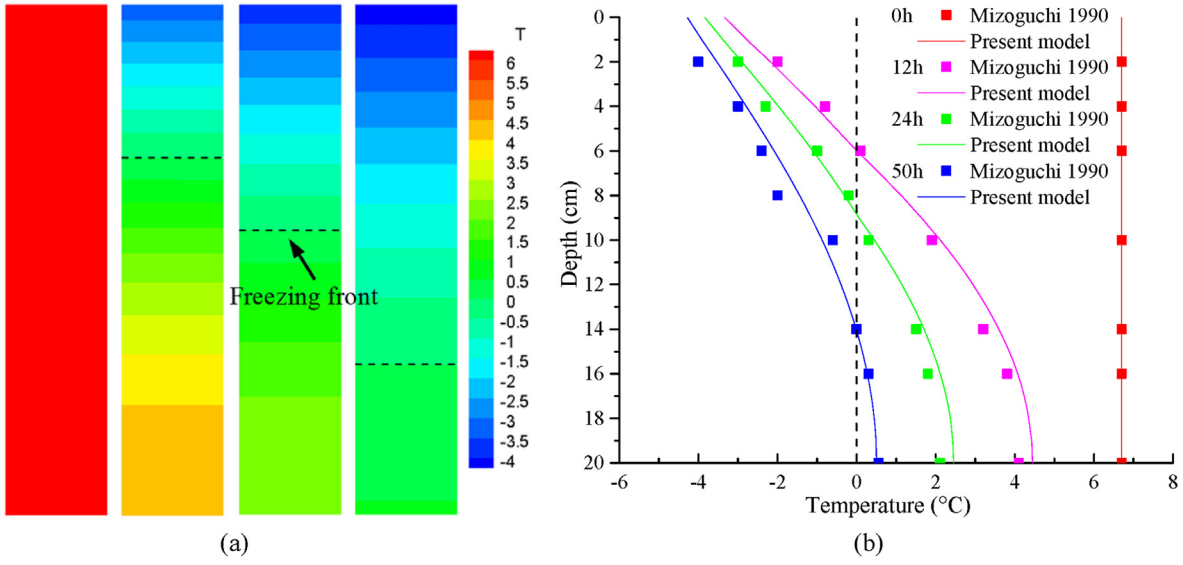

Fig. 10. (a) The temperature (T, °C) distribution at different times (t = 0 h, 12 h, 24 h and 50 h) and (b) the comparison between numerical and experimental results (Mizoguchi, 1990). The dashed line represents the freezing front.

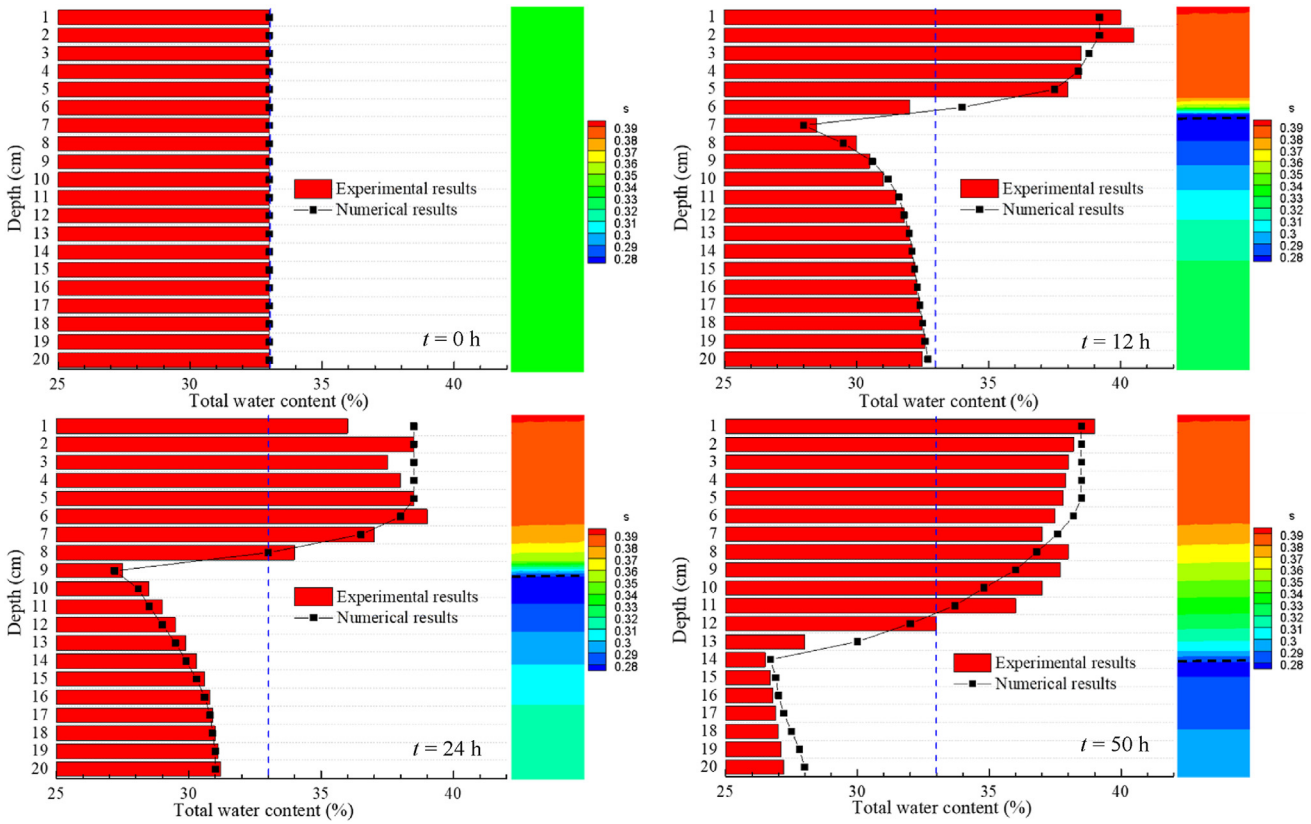

Fig. 11. Total water content (S) distribution at different times (t = 0, 12, 24 and 50 h) and comparison between numerical and experimental results. The vertical blue dashed line is the initial total water content, and the horizontal black dashed line is the freezing front.

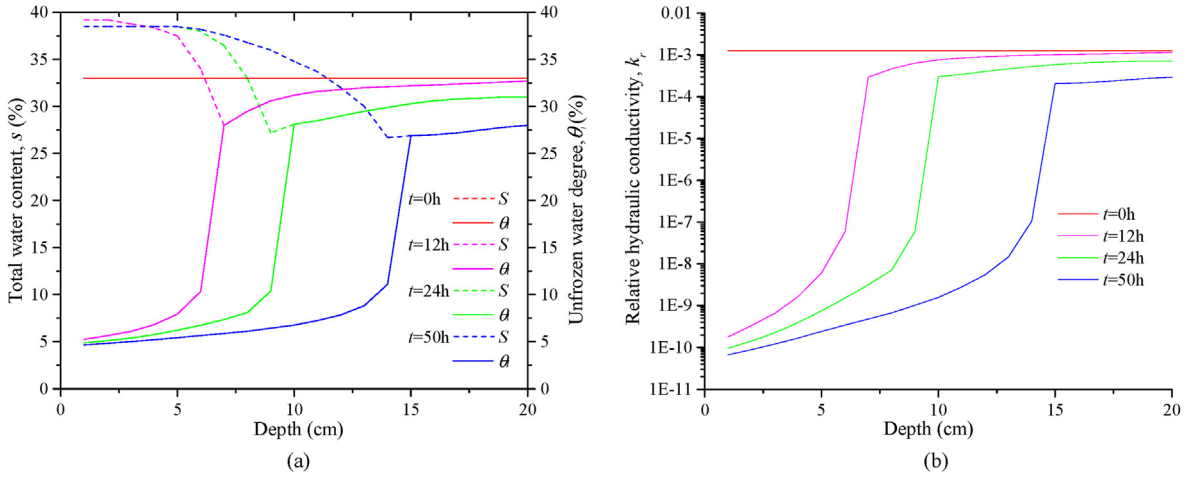

Fig. 12. (a) The distribution of the total water content (S) and the unfrozen water content (θ_l); and (b) The distribution of the relative hydraulic conductivity (k_r) at different times.

increasing in the frozen zone but decreasing in the unfrozen zone. When the temperature further decreases, more ice grows, blocking the flow channels. The permeability of the frozen zone dramatically decreases (several orders of magnitude), thus less water transfers in this zone, leading to almost constant water content in the frozen zone. A drastic change in the water content can be observed near the freezing front, where the pressure gradient and hydraulic conductivity are relatively large. Overall, the water migration is driven by cryogenic suction as ice generation but at the same time, it is retarded by the reduced permeability developed in the partially frozen rock as ice accumulation, which forms the three-zone distribution.

4.3. Test 3: frost heave of a chilled pipeline

Accurate prediction of temperature distribution, frost penetration, water migration as well as the frost heave is of great practical interest for engineering problems in cold regions. In this study case, we present a numerical example based on a field-scale experiment of ground freezing (Dallimore, 1985), in which a gas pipe with a

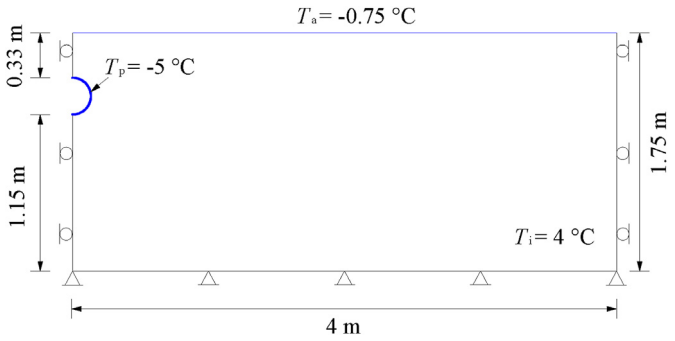

Fig. 13. Computational domain of the frost heave of a pipeline problem.

Table 4
The model parameters of the silt (after Dallimore, 1985; Bekele et al., 2017).

Parameter	Value
Young's modulus, E (MPa)	1
Poisson's ratio, ν	0.3
Porosity, n	0.4
Density, ρ (kg/m^3)	1500
Thermal conductivity, k (W/(m °C))	0.65
Specific heat capacity, c (J/(kg °C))	800
Thermal expansion coefficient, α (°C^{-1})	8×10^{-7}
Saturated hydraulic conductivity, K_s (m/s)	5×10^{-8}
Coupling parameters, η (m^{-1}), γ	0.9, 0.36

diameter of 270 mm and a length of 16 m is buried in silt and subjected to controlled thermal and hydraulic conditions (Smith and Patterson, 1989; Bekele et al., 2017). The initial temperature, T_i, is 4 °C, and the whole domain is saturated with a porosity of 0.4. During the freezing period, which lasted for 358 d, the pipe temperature, T_p, was maintained at −5 °C and the air temperature, T_a, in the hall at −0.75 °C.

A cross-section of the pipeline is considered a 2D problem, and the computational frame is only half of the cross-section due to the symmetry (Fig. 13). The following boundary conditions are defined: The bottom boundary is fixed, adiabatic, and permeable (i.e. with water supplement). The lateral boundaries are impermeable, adiabatic, and fixed horizontally. The top boundary is impermeable and unloaded. The material properties for the silt are given in Table 4, and the parameters for water/ice are the same as those in Table 1. Note that the saturation model parameters (h and g) and hydraulic conductivity model parameters (K_s and g) are estimated based on curve fitting to experimental data (Fig. 14).

4.3.1. Validation with field data

Numerical results of the variation of temperature field and vertical displacement field related to the frost heave at t = 21 d, 105 d, and 378 d are shown in Fig. 15. The temperature gradually decreases during the freezing period and frost penetration occurs from two fronts: outwards from the pipe as well as from the soil top surface downwards. At the final step (at t = 378 d), some portion of the silt still has a temperature above the freezing temperature. It can also be observed that the soil expands during the freezing process, where the largest frost heave of about 17.8 cm occurs at the centerline of the pipe and the vertical heave decreases as the distance to the pipe increases.

To better illustrate the frost penetration process, the evolution of the 0 °C isotherm, frost penetration depth and total frost heave together with experimental results are shown in Fig. 16. The monitoring points S1, S2, and S3 are located at the top surface and are 25 cm, 65 cm, and 100 cm from the centerline of the pipe, respectively. The isotherm penetrates deeply with the freezing process, and the maximum frost penetration at points S1, S2, and S3 at t = 378 d reaches 137 mm, 123 mm, and 87 mm, respectively. It is clear that the freezing front initially propagates quickly into the soil, and then its propagation slows down. As a result, the frost heave at these sites also gradually increases with increasing ice generation at the low temperature. The amount of frost heave increases nonlinearly with time, where the initial frost heave increases rapidly and then slowly. The results of multi-field simulations match the field data reasonably well (Fig. 16). It is noted that a noticeable discrepancy of the 0 °C isotherm exists around the pipe at the beginning (t = 21 d), while disappearing afterwards (t = 105 d and 378 d). This may be attributed to the prescribed temperature (−5 °C) directly applied to the pipe surface in the modeling, while the pipe temperature may gradually decrease in reality. The lower temperature assigned to the pipe surface in the modeling results in a faster temperature decrease around the pipe, however, the effect of the pipe boundary condition is eliminated when time and distance increase.

4.3.2. Effect of water migration

The maximum volume expansion that occurs at the centerline of the pipe obtained above is about 0.1 (i.e. 0.178/1.75), which is much higher than the expected value of 0.036 (i.e. 0.4 × 0.09) when all

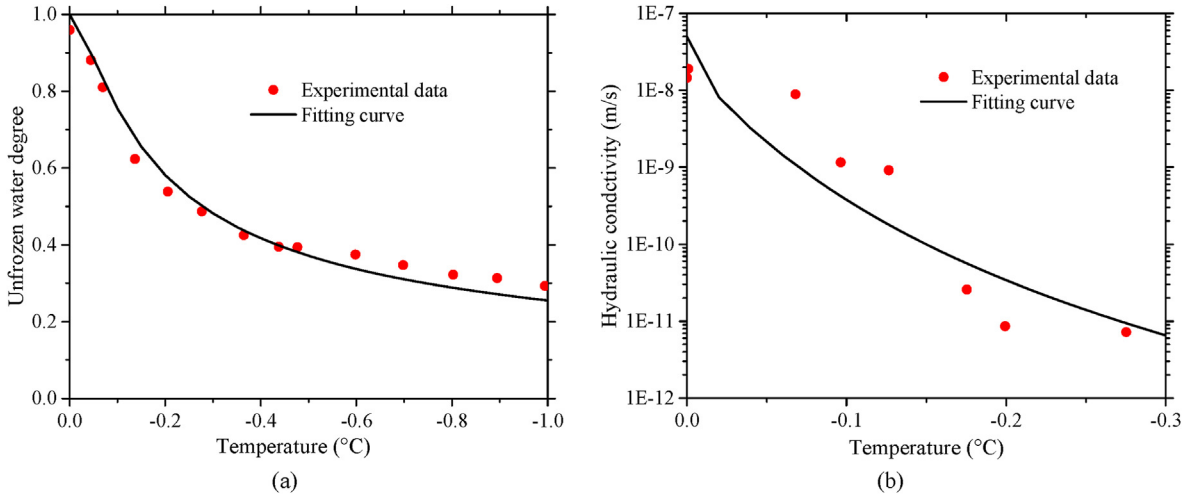

Fig. 14. Estimation of (a) saturation model parameters and (b) hydraulic conductivity model parameters based on experimental data (Dallimore, 1985).

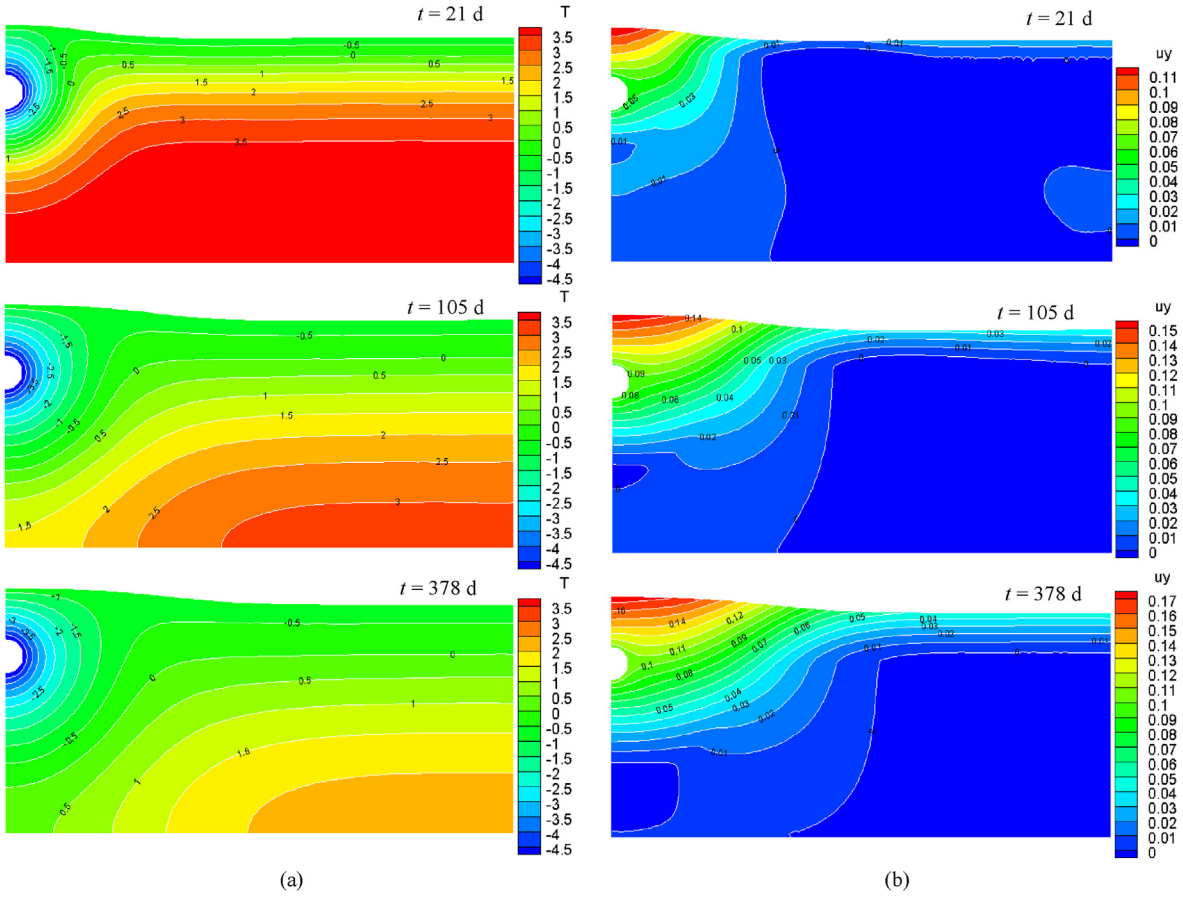

Fig. 15. (a) Temperature distribution (°C) and (b) frost heave deformation (m) at t = 21 d, 105 d, and 378 d.

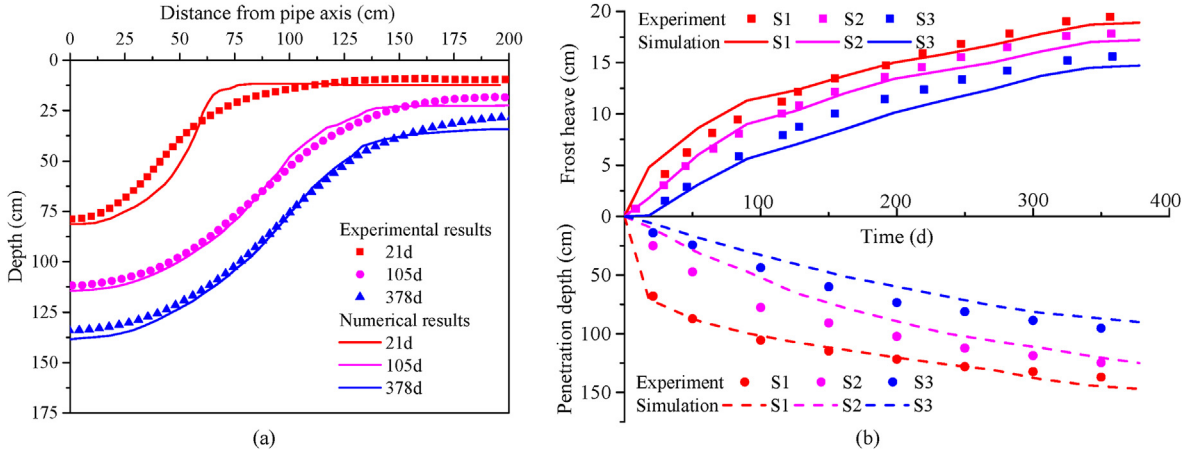

Fig. 16. Comparison of the numerical results of (a) 0 °C isotherm, (b) frost penetration depth and total frost heave with experimental results (Dallimore, 1985; Smith and Patterson, 1989).

water is assumed to be frozen into ice. Thus, the water migration from the unfrozen zone to the frozen zone is considered a major reason for the large frost heave observed in the frozen area.

To further illustrate the effect of the water migration on the temperature and frost heave distribution, as well as the necessity and efficiency of the proposed THM model. A TM coupled model, where the water migration is ignored, is conducted and compared to the results of THM model. The temperature and frost heave distribution of the TM model at t = 378 d are shown in Fig. 17. The 0 °C isotherm (i.e. freezing front) and frost heave geometry of the THM and TM models are also compared in Fig. 17c.

The variations of temperature and deformation fields follow a similar pattern, where temperature decreases from the pipe towards the far field, and a frost heave exists on the top surface. However, compared to the results of THM model, the frozen area in the TM model is slightly larger, where the maximum frost penetration (at the centerline) increases to approximately 144 mm (larger than 139 mm in the THM model). The reason can be explained by the presence of water flow from the warmer side that brings advective heat to the freezing zone in the THM model, which

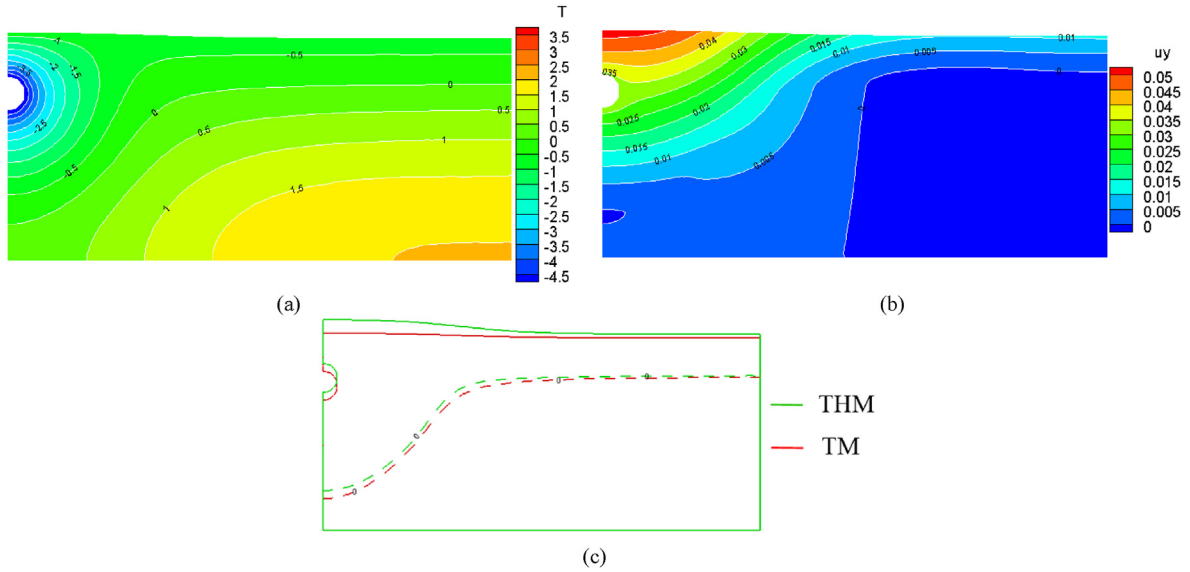

Fig. 17. (a) Temperature and (b) frost heave distributions of the TM model at t = 378 d, and (c) Comparison of 0 °C isotherm (dashed line representing the freezing front) and frost heave geometry between the THM and TM models.

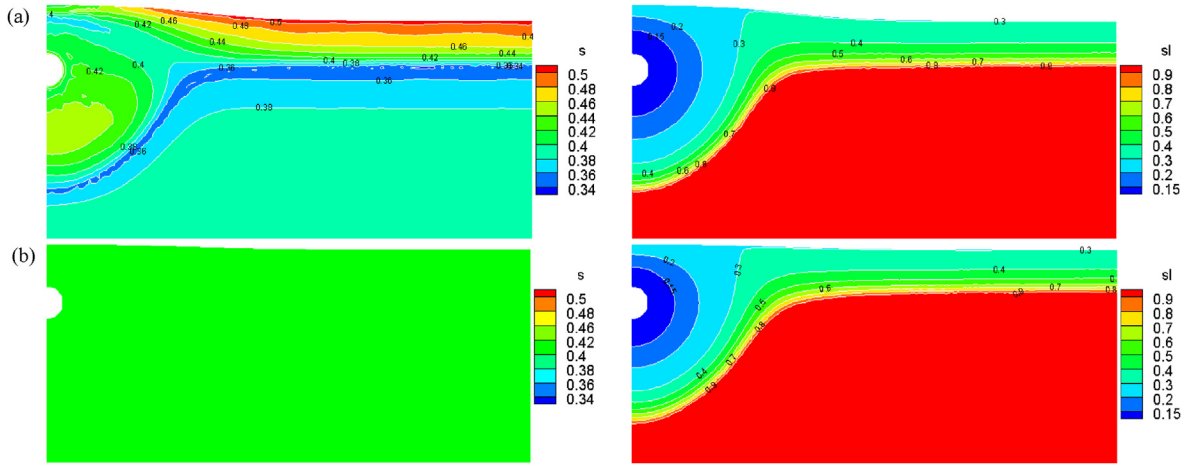

Fig. 18. Total water content (S) and unfrozen water degree (S_l) distribution at t = 378 d in (a) THM and (b) TM models.

induces a smaller freezing zone.

However, the frost heave shows a larger difference, where the maximum frost heave (at the centerline) decreases from 18.9 mm in the THM model to only 5.5 mm in the TM model. The reason can be explained by the redistribution of water content. Fig. 18 shows the distributions of the total water content and unfrozen water ratio in the simulation domain at the end of the freezing period (after 358 d). In both models, some unfrozen water remains in the areas of the frozen part, as expected from the unfrozen water content data from experiments. In THM model, water migrates to the freezing area, while there is no water flow in the TM model. Although the unfrozen water content is similar in both cases, the total water content is different. More water migrates to the freezing zone in the THM model, which means that more ice is generated, contributing to the frost heave. In addition, the migrated water also contributes to the porosity change, which is also reflected in the heave deformation.

4.3.3. *Effect of insulation material*

Thermal insulation technique is widely adopted to prevent heave frost. The effect of insulation material on frost heave is studied herein where an 8-cm thick insulation layer is installed around the pipe with a low thermal conductivity of 0.05 W/(m °C) and a specific heat capacity of 750 J/(kg °C).

The temperature field and frost heave with insulation material at the end of the freezing period (after 358 d) are shown in Fig. 19. A sharp temperature decrease (dense temperature isotherm) exists inside the insulation layer around the pipe due to the lower thermal conductivity of the insulation material. Compared to the case without the insulation material, the freezing front penetrates slower in the case with an insulation layer. The maximum depth of the freezing front (at the centerline) decreases by about 10%, from 139 mm to 126 mm. Furthermore, with the higher temperature field distributed in the sample, less water is frozen and transformed into ice (Fig. 20), thus a smaller frost heave (11.2 mm at the centerline) can be observed.

5. Discussion

Although extensive THM models (Rutqvist et al., 2001; Hudson

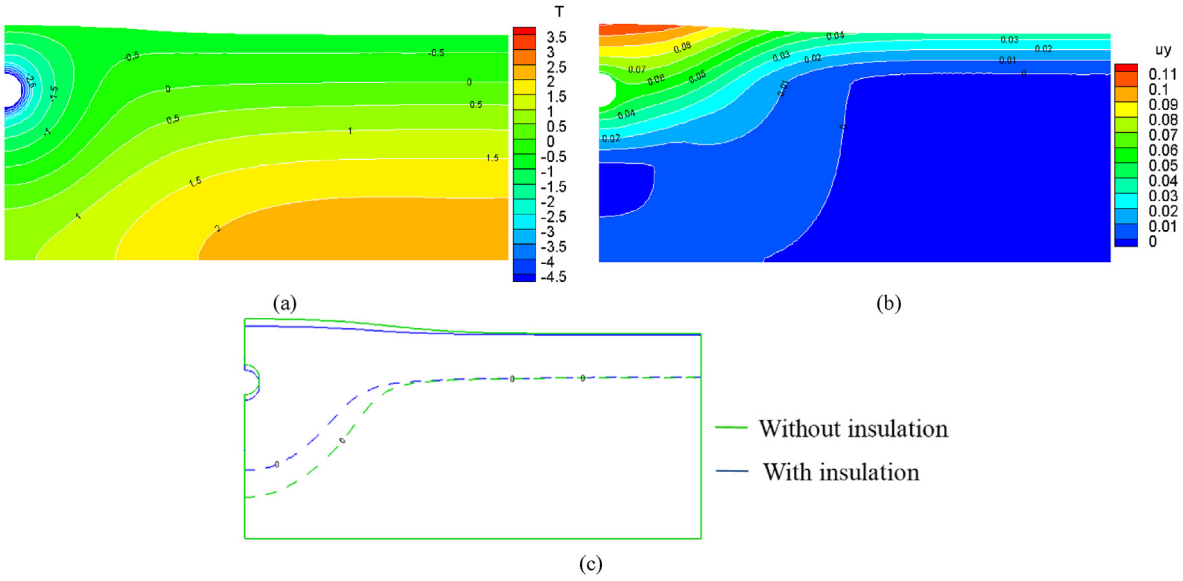

Fig. 19. (a) Temperature and (b) frost heave distributions of the model with insulation material at t = 378 d, and (c) Comparison of 0 °C isotherm (dashed line representing the freezing front) and frost heave geometry between tests with and without insulation material.

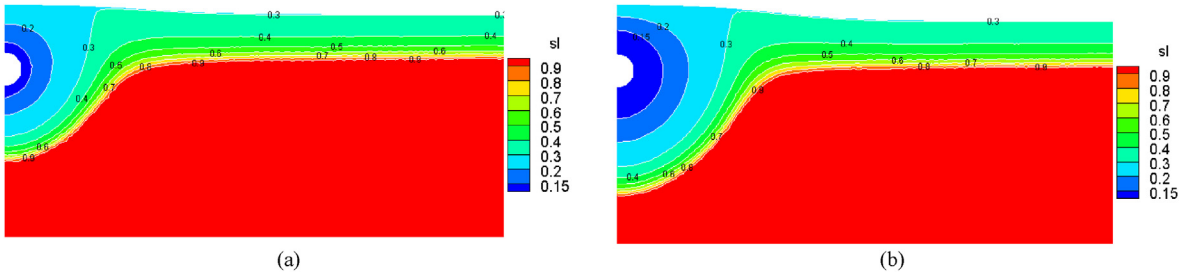

Fig. 20. Distribution of unfrozen water degree (a) with and (b) without insulation material.

et al., 2005; Tong et al., 2010; Nowak et al., 2011; Yan et al., 2022) have been recently developed for various engineering applications (e.g. geothermal energy extraction, radioactive waste storage, and oil/gas exploitation), a THM model at low-temperature conditions, considering the water/ice phase change, is still limited for geotechnical engineering in cold regions. The primary distinction is considering the water/ice phase change (PC), which introduces complicated coupling mechanisms.

This paper proposed a coupled cryogenic THM modeling framework, implemented in the FDEM, to simulate the multi-physics processes. Compared to the existing numerical methods for freezing medium, including TH (Harlan, 1973; Taylor and Luthin, 1978; Guymon et al., 1980), TM (Fremond and Mikkola, 1991; Yang et al., 2006; Michalowski and Zhu, 2006), and THM (Neaupane and Yamabe, 2001; Nishimura et al., 2009; Huang et al., 2018a) models, this cryogenic THM modeling framework well addresses all the important physical and thermodynamic phenomena and processes occurring at low temperatures, e.g. heat transfer, water/ice phase change, latent heat of phase transition, cryogenic suction, frost heave, and water migration, as well as the critical coupling parameters. Specifically, the distinct three-zone distribution that is widely observed in experiments/fields is well captured and explained by our model.

In addition, the FDEM that incorporates the advantages of both continuum and discontinuum methods is attractive for fracturing simulation. Although only continuous problems are investigated in this paper, inheriting from the advantage of FDEM, this numerical framework could be further extended to continuous-discontious problems (e.g. pre-existing discontinuities, and crack propagation). These extensions are out of the scope of this paper (which focuses on the thorough validation of the cryogenic THM framework), and will be a major uptaking in our future work to establish a systematic analysis software for complex cryogenic THM problems (e.g. frost cracking, landforms, alpine rockfall, artificial ground freezing). Moreover, three-dimensional simulation and the freezing-thaw cycles should also be developed for more realistic situations.

6. Conclusions

This work developed a coupled cryogenic THM model, implemented in the FDEM, for freezing medium. The proposed model contains three main parts: the thermal module for heat transfer, the hydraulic module for water migration, and the mechanical module for frost deformation. Mutual interaction between multi THM fields during the freezing process is inherently simulated. Particularly, compared with numerous THM coupling models, the proposed model highlighted the water/ice phase change at low temperature based on the thermodynamic theory.

The reliability and effectiveness of the proposed model have been demonstrated through a series of benchmark cases. The conceptual model has excellent capabilities in incorporating most essential phenomena and principal processes in porous media, from laboratory experiments to field observations, including heat

transfer, phase change, latent heat release, cryogenic suction, frost heave, water migration, as well as predicting the frozen depth, thermal/hydraulic/mechanical field that is of interest in practical engineering.

Specifically, the present model distinctively captured the widely observed three-zone distribution, i.e. frozen zone, unfrozen zone, and freezing zone (freezing fringe), and properly attributed the reason to the spatial and temporal variation of unfrozen water content and apparent hydraulic permeability. The water migration from the warm zone to the cold zone is driven by cryogenic suction due to ice generation but at the same time, it is retarded by the reduced permeability developed in the partially frozen rock due to ice accumulation (i.e. a trade-off between these two factors influences the water redistribution).

The results also indicate that, compared to the traditional TM model, this THM model reveals that water migration has a significant effect on the temperature and frost heave distribution. Moreover, water proofing method and thermal insulation technique, which affect the total water distribution and temperature field distribution, respectively, are useful in relieving the frost heave damage in cold regions.

Declaration of competing interest

The authors declare that they have no known competing financial interests or personal relationships that could have appeared to influence the work reported in this paper.

Acknowledgments

This work was supported by the Natural Sciences and Engineering Research Council of Canada (NSERC) Discovery Grants 341275, NSERC CRDPJ 543894-19, and NSERC/Energi Simulation Industrial Research Chair program. K.R. Aboayanah is grateful for the funding he received from Lassonde International Graduate Scholarship in Mining at the University of Toronto. Q. Zhao is supported by the FCE Start-up Fund for New Recruits at the Hong Kong Polytechnic University (P0034042) and the Early Career Scheme and the General Research Fund Scheme of the Research Grants Council of the Hong Kong SAR, China (Project Nos. PolyU 25220021 and PolyU 15227222).

References

Arzanfudi, M.M., Al-Khoury, R., 2018. Freezing-thawing of porous media: an extended finite element approach for soil freezing and thawing. Adv. Water Resour. 119, 210–226.
Bai, R., Lai, Y., Pei, W., Zhang, M., 2020. Investigation on frost heave of saturated–unsaturated soils. Acta Geotech 15, 3295–3306.
Bekele, Y.W., Kyokawa, H., Kvarving, A.M., Kvamsdal, T., Nordal, S., 2017. Isogeometric analysis of THM coupled processes in ground freezing. Comput. Geotech. 88, 129–145.
Burt, T.P., Williams, P.J., 1976. Hydraulic conductivity in frozen soils. Earth Surf. Process. Landforms 1, 349–360.
Cai, H., Li, S., Liang, Y., Yao, Z., Cheng, H., 2019. Model test and numerical simulation of frost heave during twin-tunnel construction using artificial ground-freezing technique. Comput. Geotech. 115, 103155.
Coussy, O., 2005. Poromechanics of freezing materials. J. Mech. Phys. Solid. 53, 1689–1718.
Coussy, O., Monteiro, P.J.M., 2008. Poroelastic model for concrete exposed to freezing temperatures. Cement Concr. Res. 38, 40–48.
Dallimore, S.R., 1985. Observations and Predictions of Frost Heave Around a Chilled Pipeline. Carleton University.
Deprez, M., Kock, T. de, Schutter, G. de, Cnudde, V., 2020. A review on freeze-thaw action and weathering of rocks. Earth Sci. Rev. 203, 103143.
Duca, S., Alonso, E.E., Scavia, C., 2015. A permafrost test on intact gneiss rock. Int. J. Rock Mech. Min. Sci. 77, 142–151.
Fischer, L., 2009. Slope Instabilities on Perennially Frozen and Glacierised Rock Walls: Multi-Scale Observations, Analyses and Modelling. University of Zurich.
Fredlund, D.G., Rahardjo, H., 1993. Soil Mechanics for Unsaturated Soils. Wiley, New York.
Fremond, M., Mikkola, M., 1991. Thermomechanical modeling of freezing soil. In: International Symposium on Ground Freezing, pp. 17–24.
Fukuda, D., Mohammadnejad, M., Liu, H., Zhang, Q., Zhao, J., Dehkhoda, S., Chan, A., Kodama, J., Fujii, Y., 2020. Development of a 3D hybrid finite-discrete element simulator based on GPGPU-parallelized computation for modelling rock fracturing under quasi-static and dynamic loading conditions. Rock Mech. Rock Eng. 53, 1079–1112.
Gruber, S., Haeberli, W., 2007. Permafrost in steep bedrock slopes and its temperature-related destabilization following climate change. J. Geophys. Res.: Earth Surf. 112, 301.
Guymon, G.L., Hromadka, T.V., Berg, R.L., 1980. A one dimensional frost heave model based upon simulation of simultaneous heat and water flux. Cold Reg. Sci. Technol. 3, 253–262.
Hansson, K., Šimůnek, J., Mizoguchi, M., Lundin, L.-C., Genuchten, M.T., 2004. Water flow and heat transport in frozen soil: numerical solution and freeze–thaw applications. Vadose Zone J. 3, 693–704.
Harlan, R.L., 1973. Analysis of coupled heat-fluid transport in partially frozen soil. Water Resour. Res. 9, 1314–1323.
Harris, C., Arenson, L.U., Christiansen, H.H., Etzelmüller, B., Frauenfelder, R., Gruber, S., Haeberli, W., Hauck, C., Hölzle, M., Humlum, O., Isaksen, K., Kääb, A., Kern-Lütschg, M.A., Lehning, M., Matsuoka, N., Murton, J.B., Nötzli, J., Phillips, M., Ross, N., Seppälä, M., Springman, S.M., Vonder Mühll, D., 2009. Permafrost and climate in Europe: monitoring and modelling thermal, geomorphological and geotechnical responses. Earth Sci. Rev. 92, 117–171.
Huang, S., Liu, Q., Cheng, A., Liu, Y., Liu, G., 2018a. A fully coupled thermo-hydro-mechanical model including the determination of coupling parameters for freezing rock. Int. J. Rock Mech. Min. Sci. 103, 205–214.
Huang, S., Liu, Q., Liu, Y., Kang, Y., Cheng, A., Ye, Z., 2018b. Frost heaving and frost cracking of elliptical cavities (fractures) in low-permeability rock. Eng. Geol. 234, 1–10.
Huang, S., Lu, Z., Ye, Z., Xin, Z., 2020. An elastoplastic model of frost deformation for the porous rock under freeze-thaw. Eng. Geol. 278, 105820.
Hudson, J.A., Stephansson, O., Andersson, J., 2005. Guidance on numerical modelling of thermo-hydro-mechanical coupled processes for performance assessment of radioactive waste repositories. Int. J. Rock Mech. Min. Sci. 42, 850–870.
Jing, L., Hudson, J.A., 2002. Numerical methods in rock mechanics. Int. J. Rock Mech. Min. Sci. 39, 409–427.
Johannesson, B., 2010. Dimensional and ice content changes of hardened concrete at different freezing and thawing temperatures. Cement Concr. Compos. 32, 73–83.
Kang, Y., Liu, Q., Huang, S., 2013. A fully coupled thermo-hydro-mechanical model for rock mass under freezing/thawing condition. Cold Reg. Sci. Technol. 95, 19–26.
Knight, E.E., Rougier, E., Lei, Z., Euser, B., Chau, V., Boyce, S.H., Gao, K., Okubo, K., Froment, M., 2020. HOSS: an implementation of the combined finite-discrete element method. Comput. Part. Mech. 7, 765–787.
Konrad, J.-M., Morgenstern, N.R., 1980. A mechanistic theory of ice lens formation in fine-grained soils. Can. Geotech. J. 17, 473–486.
Kurylyk, B.L., Watanabe, K., 2013. The mathematical representation of freezing and thawing processes in variably-saturated, non-deformable soils. Adv. Water Resour. 60, 160–177.
Lai, Y., Pei, W., Zhang, M., Zhou, J., 2014. Study on theory model of hydro-thermal–mechanical interaction process in saturated freezing silty soil. Int. J. Heat Mass Tran. 78, 805–819.
Lei, Q., Latham, J.-P., Xiang, J., Tsang, C.-F., Lang, P., Guo, L., 2014. Effects of geomechanical changes on the validity of a discrete fracture network representation of a realistic two-dimensional fractured rock. Int. J. Rock Mech. Min. Sci. 70, 507–523.
Lisjak, A., Kaifosh, P., He, L., Tatone, B.S.A., Mahabadi, O.K., Grasselli, G., 2017. A 2D, fully-coupled, hydro-mechanical, FDEM formulation for modelling fracturing processes in discontinuous, porous rock masses. Comput. Geotech. 81, 1–18.
Lisjak, A., Mahabadi, O.K., He, L., Tatone, B.S.A., Kaifosh, P., Haque, S.A., Grasselli, G., 2018. Acceleration of a 2D/3D finite-discrete element code for geomechanical simulations using General Purpose GPU computing. Comput. Geotech. 100, 84–96.
Liu, Z., Yu, X., 2011. Coupled thermo-hydro-mechanical model for porous materials under frost action: theory and implementation. Acta Geotech 6, 51–65.
Lu, J.-F., Tan, Y.-P., Wang, J.-H., 2011. A phase field model for the freezing saturated porous medium. Int. J. Eng. Sci. 49, 768–780.
Lv, Z., Xia, C., Li, Q., 2018. Experimental and numerical study on frost heave of saturated rock under uniform freezing conditions. J. Geophys. Eng. 15, 593–612.
Lv, Z., Xia, C., Li, Q., Si, Z., 2019. Empirical frost heave model for saturated rock under uniform and unidirectional freezing conditions. Rock Mech. Rock Eng. 52, 955–963.
Lv, Z., Xia, C., Wang, Y., Lin, Z., 2020. Frost heave and freezing processes of saturated rock with an open crack under different freezing conditions. Front. Struct. Civ. Eng. 14, 947–960.
Matsuoka, N., Murton, J., 2008. Frost weathering: recent advances and future directions. Permafr. Periglac. Process. 19, 195–210.
Michalowski, R.L., Zhu, M., 2006. Frost heave modelling using porosity rate function. Int. J. Numer. Anal. Methods GeoMech. 30, 703–722.
Mizoguchi, M., 1990. Water, Heat and Salt Transport in Freezing Soil. University of Tokyo.
Mu, S., Ladanyi, B., 1987. Modelling of coupled heat, moisture and stress field in freezing soil. Cold Reg. Sci. Technol. 14, 237–246.

Munjiza, A., 2004. The Combined Finite-Discrete Element Method. John Wiley, Chichester.
Na, S., Sun, W., 2017. Computational thermo-hydro-mechanics for multiphase freezing and thawing porous media in the finite deformation range. Comput. Methods Appl. Mech. Eng. 318, 667–700.
Na, S.H., 2018. Multiscale Thermo-Hydro-Mechanical-Chemical Coupling Effects for Fluid-Infiltrating Crystalline Solids and Geomaterials: Theory, Implementation, and Validation. Columbia University.
Nassar, I.N., Horton, R., 1992. Simultaneous transfer of heat, water, and solute in porous media: I. Theoretical development. Soil Sci. Soc. Am. J. 56, 1350–1356.
Neaupane, K.M., Yamabe, T., 2001. A fully coupled thermo-hydro-mechanical nonlinear model for a frozen medium. Comput. Geotech. 28, 613–637.
Neville, A.M., 1995. Properties of Concrete, fourth ed. Longman, London.
Nishimura, S., Gens, A., Olivella, S., Jardine, R.J., 2009. THM-coupled finite element analysis of frozen soil: formulation and application. Geotechnique 59, 159–171.
Nowak, T., Kunz, H., Dixon, D., Wang, W., Görke, U.-J., Kolditz, O., 2011. Coupled 3-D thermo-hydro-mechanical analysis of geotechnological in situ tests. Int. J. Rock Mech. Min. Sci. 48, 1–15.
Obu, J., Westermann, S., Bartsch, A., Berdnikov, N., Christiansen, H.H., Dashtseren, A., Delaloye, R., Elberling, B., Etzelmüller, B., Kholodov, A., Khomutov, A., Kääb, A., Leibman, M.O., Lewkowicz, A.G., Panda, S.K., Romanovsky, V., Way, R.G., Westergaard-Nielsen, A., Wu, T., Yamkhin, J., Zou, D., 2019. Northern Hemisphere permafrost map based on TTOP modelling for 2000–2016 at 1 km2 scale. Earth Sci. Rev. 193, 299–316.
Rouabhi, A., Jahangir, E., Tounsi, H., 2018. Modeling heat and mass transfer during ground freezing taking into account the salinity of the saturating fluid. Int. J. Heat Mass Tran. 120, 523–533.
Rutqvist, J., Börgesson, L., Chijimatsu, M., Nguyen, T.S., Jing, L., Noorishad, J., Tsang, C.-F., 2001. Coupled thermo-hydro-mechanical analysis of a heater test in fractured rock and bentonite at Kamaishi Mine — comparison of field results to predictions of four finite element codes. Int. J. Rock Mech. Min. Sci. 38, 129–142.
Saito, H., Šimůnek, J., Mohanty, B.P., 2006. Numerical analysis of coupled water, vapor, and heat transport in the vadose zone. Vadose Zone J. 5, 784–800.
Smith, M.W., Patterson, D.E., 1989. Detailed observations on the nature of frost heaving at a field scale. Can. Geotech. J. 26, 306–312.
Streletskiy, D.A., Shiklomanov, N.I., Nelson, F.E., 2018. Permafrost, infrastructure, and climate change: a GIS-based Landscape approach to geotechnical modeling. Arctic Antarct. Alpine Res. 44, 368–380.
Stuurop, J.C., van der Zee, S.E.A.T.M., Voss, C.I., French, H.K., 2021. Simulating water and heat transport with freezing and cryosuction in unsaturated soil: comparing an empirical, semi-empirical and physically-based approach. Adv. Water Resour. 149, 103846.
Suh, H.S., Sun, W., 2022. Multi-phase-field microporomechanics model for simulating ice-lens growth in frozen soil. Int. J. Numer. Anal. Methods GeoMech. 46, 2307–2336.
Sun, L., Grasselli, G., Liu, Q., Tang, X., Abdelaziz, A., 2022c. The role of discontinuities in rock slope stability: insights from a combined finite-discrete element simulation. Comput. Geotech. 147, 104788.
Sun, L., Liu, Q., Abdelaziz, A., Tang, X., Grasselli, G., 2022b. Simulating the entire progressive failure process of rock slopes using the combined finite-discrete element method. Comput. Geotech. 141, 104557.
Sun, L., Liu, Q., Grasselli, G., Tang, X., 2020. Simulation of thermal cracking in anisotropic shale formations using the combined finite-discrete element method. Comput. Geotech. 117, 103237.
Sun, L., Liu, Q., Tao, S., Grasselli, G., 2022a. A novel low-temperature thermo-mechanical coupling model for frost cracking simulation using the finite-discrete element method. Comput. Geotech. 152, 105045.
Sun, L., Tang, X., Abdelaziz, A., Liu, Q., Grasselli, G., 2023b. Stability analysis of reservoir slopes under fluctuating water levels using the combined finite-discrete element method. Acta Geotech 52, 561.
Sun, L., Tao, S., Liu, Q., 2023a. Frost crack propagation and interaction in Fissured rocks subjected to freeze–thaw cycles: experimental and numerical studies. Rock Mech. Rock Eng. 56, 1077–1097.
Sweidan, A.H., Heider, Y., Markert, B., 2020. A unified water/ice kinematics approach for phase-field thermo-hydro-mechanical modeling of frost action in porous media. Comput. Methods Appl. Mech. Eng. 372, 113358.
Tan, X., Chen, W., Liu, H., Wang, L., Ma, W., Chan, A.H.C., 2018. A unified model for frost heave pressure in the rock with a penny-shaped fracture during freezing. Cold Reg. Sci. Technol. 153, 1–9.
Tan, X., Chen, W., Tian, H., Cao, J., 2011. Water flow and heat transport including ice/water phase change in porous media: numerical simulation and application. Cold Reg. Sci. Technol. 68, 74–84.
Tan, X., Chen, W., Wu, G., Yang, J., 2013. Numerical simulations of heat transfer with ice–water phase change occurring in porous media and application to a cold-region tunnel. Tunn. Undergr. Space Technol. 38, 170–179.
Taylor, G.S., Luthin, J.N., 1978. A model for coupled heat and moisture transfer during soil freezing. Can. Geotech. J. 15, 548–555.
Tong, F., Jing, L., Zimmerman, R.W., 2010. A fully coupled thermo-hydro-mechanical model for simulating multiphase flow, deformation and heat transfer in buffer material and rock masses. Int. J. Rock Mech. Min. Sci. 47, 205–217.
Tounsi, H., Rouabhi, A., Tijani, M., Guérin, F., 2019. Thermo-hydro-mechanical modeling of artificial ground freezing: application in mining engineering. Rock Mech. Rock Eng. 52, 3889–3907.
van Genuchten, M.T., 1980. A closed-form equation for predicting the hydraulic conductivity of unsaturated soils. Soil Sci. Soc. Am. J. 44, 892–898.
Weng, L., Wu, Z., Liu, Q., Chu, Z., Zhang, S., 2021. Evolutions of the unfrozen water content of saturated sandstones during freezing process and the freeze-induced damage characteristics. Int. J. Rock Mech. Min. Sci. 142, 104757.
Williams, P.J., Smith, M.W., 2009. The Frozen Earth. Cambridge University Press.
Wu, D., Lai, Y., Zhang, M., 2015. Heat and mass transfer effects of ice growth mechanisms in a fully saturated soil. Int. J. Heat Mass Tran. 86, 699–709.
Wu, W., Wan, T., Yang, Y., Zheng, H., 2022a. Three-dimensional numerical manifold formulation with continuous nodal gradients for dynamics of elasto-plastic porous media. Comput. Methods Appl. Mech. Eng. 388, 114203.
Wu, W., Yang, Y., Zheng, H., 2020a. Enriched mixed numerical manifold formulation with continuous nodal gradients for dynamics of fractured poroelasticity. Appl. Math. Model. 86, 225–258.
Wu, W., Yang, Y., Zheng, H., 2020b. Hydro-mechanical simulation of the saturated and semi-saturated porous soil–rock mixtures using the numerical manifold method. Comput. Methods Appl. Mech. Eng. 370, 113238.
Wu, W., Yang, Y., Zheng, H., Zhang, L., Zhang, N., 2022b. Numerical manifold computational homogenization for hydro-dynamic analysis of discontinuous heterogeneous porous media. Comput. Methods Appl. Mech. Eng. 388, 114254.
Wu, W., Zheng, H., Yang, Y., 2019. Enriched three-field numerical manifold formulation for dynamics of fractured saturated porous media. Comput. Methods Appl. Mech. Eng. 353, 217–252.
Xia, C., Lv, Z., Li, Q., Huang, J., Bai, X., 2018. Transversely isotropic frost heave of saturated rock under unidirectional freezing condition and induced frost heaving force in cold region tunnels. Cold Reg. Sci. Technol. 152, 48–58.
Yan, C., Fan, H., Huang, D., Wang, G., 2021. A 2D mixed fracture–pore seepage model and hydromechanical coupling for fractured porous media. Acta Geotech 16, 3061–3086.
Yan, C., Jiao, Y.-Y., 2019. FDEM-TH3D: a three-dimensional coupled hydrothermal model for fractured rock. Int. J. Numer. Anal. Methods GeoMech. 43, 415–440.
Yan, C., Xie, X., Ren, Y., Ke, W., Wang, G., 2022. A FDEM-based 2D coupled thermal-hydro-mechanical model for multiphysical simulation of rock fracturing. Int. J. Rock Mech. Min. Sci. 149, 104964.
Yang, P., Ke, J.-m., Wang, J.G., Chow, Y.K., Zhu, F.-b., 2006. Numerical simulation of frost heave with coupled water freezing, temperature and stress fields in tunnel excavation. Comput. Geotech. 33, 330–340.
Zhang, X., Wang, Q., Yu, T., Wang, G., Wang, W., 2018. Numerical study on the multifield mathematical coupled model of hydraulic-thermal-salt-mechanical in saturated freezing saline soil. Int. J. GeoMech. 18, 4018064.
Zhang, X., Wu, Y., Zhai, E., Ye, P., 2021. Coupling analysis of the heat-water dynamics and frozen depth in a seasonally frozen zone. J. Hydrol. 593, 125603.
Zhelnin, M., Kostina, A., Prokhorov, A., Plekhov, O., Semin, M., Levin, L., 2022. Coupled thermo-hydro-mechanical modeling of frost heave and water migration during artificial freezing of soils for mineshaft sinking. J. Rock Mech. Geotech. Eng. 14, 537–559.
Zhou, X., Zhou, J., Kinzelbach, W., Stauffer, F., 2014. Simultaneous measurement of unfrozen water content and ice content in frozen soil using gamma ray attenuation and TDR. Water Resour. Res. 50, 9630–9655.
Zhou, Y., Zhou, G., 2012. Intermittent freezing mode to reduce frost heave in freezing soils - experiments and mechanism analysis. Can. Geotech. J. 49, 686–693.

Dr. Lei Sun obtained his BEng degree from Sichuan University in 2014 and PhD from Wuhan University in 2020. Now he is working as a postdoctoral fellow at the University of Toronto. His research interests lie in multifield coupling and computational mechanic sciences, which are applied to critical energy and storage applications (e.g. CO_2 geological storage, geothermal energy extraction, radioactive waste storage, and oil/gas exploitation). Recently, he aims to develop a robust THMC coupling model based on the combined finite-discrete element method (FDEM).

Dr. Qi Zhao is an Assistant Professor at the Civil and Environmental Engineering Department at the Hong Kong Polytechnic University (PolyU). He obtained his PhD at the University of Toronto and then worked as a postdoc at the University of Toronto and UC Berkeley before joining PolyU. He is a recipient of the Leopold Müller Award by the Austrian Society for Geomechanics and the Dr N.G.W. Cook PhD Dissertation Award by the American Rock Mechanics Association (ARMA). He was selected to be a Future Leader of ARMA in 2021. He chaired and hosted the 2023 ARMA East Asia Geomechanics Workshop.